Hypersonic Heat Transfer and Anisotropic Visualization with a Higher Order Discontinuous Galerkin Finite Element Method

by

Douglas J. Quattrochi

B.S., Massachusetts Institute of Technology (2004)

Submitted to the Department of Aeronautics and Astronautics
in partial fulfillment of the requirements for the degree of

Master of Science in Aeronautics and Astronautics

at the

MASSACHUSETTS INSTITUTE OF TECHNOLOGY

June 2006

Author ....
Department of Aeronautics and Astronautics
February 17, 2006

Certified by.. .....
David Darmofal
Associate Professor
Thesis Supervisor

Accepted by ....
Jaime Peraire
Professor of Aeronautics and Astronautics
Chair, Committee on Graduate Students

AERO

Hypersonic Heat Transfer and Anisotropic Visualization with a Higher Order Discontinuous Galerkin Finite Element Method

by

Douglas J. Quattrochi

Submitted to the Department of Aeronautics and Astronautics
on February 17, 2006, in partial fulfillment of the
requirements for the degree of
Master of Science in Aeronautics and Astronautics

Abstract

Higher order discretizations of the Navier-Stokes equations promise greater accuracy than conventional computational aerodynamics methods. In particular, the discontinuous Galerkin (DG) finite element method has $\mathcal{O}(h^{p+1})$ design accuracy and allows for subcell resolution of shocks. This work furthers the DG finite element method in two ways. First, it demonstrates the results of DG when used to predict heat transfer to a cylinder in a hypersonic flow. The strong shock is captured with a Laplacian artificial viscosity term. On average, the results are in agreement with an existing hypersonic benchmark. Second, this work improves the visualization of the higher order polynomial solutions generated by DG with an adaptive display algorithm. The new algorithm results in more efficient displays of higher order solutions, including the hypersonic flow solutions generated here.

Thesis Supervisor: David Darmofal
Title: Associate Professor

Acknowledgments

I often think clearly, but reason alone would have been insufficient to produce this thesis on such a compressed timeline. Experience, too, was needed, and promptly shared with me at my incessant requests by my collaborators in Project-X: Krzysztof Fidkowski, Todd Oliver, and Garrett Barter. Enough cannot be said by way of appreciation for their alacritous and enormously helpful advice, and for their work, of which this is a continuation. Similarly crucial experience was shared by my advisor, David Darmofal, who knew enough about CFD and project planning to answer my request for a hypersonics project with something that would push against the limits of time and computational space; this is exactly how I prefer to operate. Moreover, his precise and principled feedback was absolutely essential to my education and to the compilation of this text. To Bob Haimes I owe a beautiful way to describe my limited ability to use C pointers: "programming by Brownian motion." I'd like to think that in the course of our discussions some of his programming pizazz has rubbed off on me. Also, I would be somewhat remiss not to mention J. Peter Whitney. From time to time he would casually ask me how this work was going, and whatever I managed to grumble at him, thwack it back with a startlingly incisive and fruitful question. I also acknowledge Mike Park, whose generous consultations in the early stages of this work made possible the acquisition of the Langley cylinder grid. And not least of all, I have benefitted greatly from the experience of my parents, who were my first teachers, and who knew enough about merit to fund nearly my entire education, and much else, no questions asked. It pleases me to acknowledge this help beyond what may already appear in the footnotes or the references, which is another long list, indeed.

A portion of this work was supported by NASA Langley under NAG-1-02037. This, last but not least, is most gratefully acknowledged as well.

Contents

List of Figures

List of Tables

Chapter 1

Introduction

1.1 The Origins of Blunt Body Computation

A fundamental question in the design of any hypersonic flight vehicle is, "how hot will it get?" The answer to this question usually motivates a follow-on, "how can it be prevented from getting that hot?"

These two questions first received serious attention in the 1950's from ballistic missile designers [42]. When their slender, pointed missile designs were tested in hypersonic flows, they invariably found the answer to the first question to be, "hot enough to melt." Computers were applied to the problem to find a survivable shape, but decades of experience in reducing drag and streamlining vehicles had left the programmers trapped in the mindset "narrower is better." The answer always came back "make it narrower," and the design always failed [33].

In 1952, National Advisory Committee for Aeronautics scientist H. Julian Allen, working at the Ames Aeronautical Laboratory, realized that a blunted nose would fare far better in high speed flight than the slimmest, sleekest missile designs at the time[1] [1]. In fact, the heat transfer to the nose of an object traveling much faster than the speed of sound is inversely proportional to the square root of the radius of curvature [2]. So as a body is blunted and its leading radius of curvature increased, the heat transfer to the body is decreased. Unlike a pointed design, in which a shock sits on the body and the dissipated thermal energy is transmitted directly to the vehicle, a blunted body forms a detached shock that redirects enough of the thermal energy to the air flow for a heat sink to be effective.

[1]The work was set to paper with Alfred J. Eggers and remained classified until published six years later.

The so-called "blunt body" design became the best answer to the second question, but in so doing considerably confused the answer to the first. Even for simple shapes, such as cylinders or spheres, the flow around a blunt body has no analytical solution. The subsonic flow found in the stagnation region, which is mathematically elliptic, can be analytically coupled to the supersonic flow around it, which is mathematically hyperbolic, only if the boundaries between the two regions are known in advance. Knowledge of the boundaries comes only from the full solution.

The breakthrough came from computation. In 1966, Moretti and Abbett proposed applying computational techniques to the *unsteady* flow problem, which was everywhere hyperbolic [41]. With this approach, the unsteady problem converges to the steady-state solution, with its supersonic and subsonic regions appearing automatically. Their original results were consistent with the numerical data published at the time, as well as with analytical relations for the change in state across a shock. While other specialized numerical methods had also solved the "blunt body problem," the Moretti and Abbett idea – solving a steady problem with an unsteady computation – is generally applicable. It is used still, including in the present work.

1.2 The Search for Better CFD

Since then a tremendous effort has been made to apply CFD to increasingly detailed and difficult problems, hypersonic heat transfer being but one, and to produce increasingly accurate results. The methods typically used in aerospace applications today are second-order accurate, meaning that when solving smooth flow problems, as the grid spacing, h, decreases, the error decreases as $\mathcal{O}(h^2)$. For flows with shocks or other discontinuities, convergence will be $\mathcal{O}(h)$.

Many modern CFD implementations were recently compared against one another and against experiment in two workshops to predict the drag of a passenger jet in turbulent flow [36, 39]. A sequence of three grids were used: one coarse, one medium, and one fine. According to [36], "the medium grid was sized to be sufficient for industry drag prediction." The analysis of the results in [59] shows that the variation between implementations is significant. Additionally, the sequence of grids could not be used to arrive at an asymptotically

grid-independent solution. The variation not only between methods but also between grids casts doubt on whether industry's $\mathcal{O}(h^2)$ solutions are actually sufficient for industrial work.

The uncertainty of the results with industry-standard methods increases the allure of even higher order discretizations as a means to achieve grid-independence with less computational effort[2]. Higher order finite difference [37, 63, 68, 70] and finite volume [65] methods have already been pursued. The salient problem with higher order accuracy in most of these implementations is the extended coupling between grid points. This leads to problems with stability, memory, and parallelization, and is discussed further in [19].

Discontinuous Galerkin (DG) finite element methods hold an advantage in this regard: the ability to incorporate higher order accurate machinery entirely within an element. With this discretization, the only coupling between grid elements comes from the inter-element fluxes. This allows for the benefits of (at best) $\mathcal{O}(h^{p+1})$ accuracy [51], where p is the order of the solution basis, without the problems of extended stencils. Explicit solution methods for DG discretizations have been used to simulate the shocks found in hyperbolic problems [16], as well as to simulate the boundary layers found in elliptic problems [6]. Implicit solution methods have been developed more recently for DG discretizations of both hyperbolic and elliptic problems [5, 19, 20, 21, 43].

1.3 Difficulties with Hypersonics

Long after Moretti and Abbett, the simulation of hypersonic flow fields of interest is still difficult. The problems do not disappear with higher order methods.

At the most fundamental level, the physical models needed to describe the flow – for instance, high temperature effects – remain case specific [18], or worse, poorly validated. It is difficult to validate new models by comparing computation to experiment because of experimental error, 3D effects in what appear to be 2D simulations [22], and the need to compute flows not only in the test section but also throughout the entire facility [24, 66].

The most crucial of the problems with modeling is accurate prediction of the laminar-turbulent transition [24, 66]. Without this, vehicles will continue to be severely overbuilt for design conditions and in risk of failure when off-design. The example given in [66] is that

[2]In general, higher order means that the error decreases as $\mathcal{O}(h^{>1})$. "Even higher" order means higher than those used in the drag prediction workshop, some of which were $\mathcal{O}(h^2)$.

a 1 mm uncertainty in the placement of protective tiling can lead to a 5 km uncertainty in the altitude at which transition happens over the tile. Studies of transition and turbulent heating in [7, 32] show how either laminar or turbulent heat transfer can be predicted to within experimental accuracy, but the sometimes large transition region is not well modeled at all. The error in transition heat transfer is as large as a factor of three.

Even with simplified physics, the implementation of a hypersonic flow model is still problematic. Gnoffo lists three factors that have a large impact on the quality of a hypersonic flow solution [24]. The first of these is grid alignment. A grid aligned well with a shock produces less artificial dissipation than a badly aligned grid. This prevents the shock from being smeared over many elements and reduces the amount of numerical error that washes downstream. Good alignment may nevertheless aggravate a problem with certain fluxes, particularly the Roe flux, that converge to spurious solutions in the presence of strong shocks [22]. Possible fixes have been suggested in [26, 53].

The second factor is grid resolution. A grid should be finely resolved through shocks and boundary layers. To keep the costs of a fine grid at a minimum, adaptive refinement techniques, which generally require unstructured grids, should be used wherever possible [61]. The use of unstructured grids is consistent with another goal, namely, the ability to mesh arbitrarily complex geometries. But adaptation is not without its own problems. In the finite difference context, adaptation introduces spacing irregularities that may introduce new errors [68]. It may also be that some degree of mesh orthogonality is required across a shock [24], and for the calculation of surface gradients, regularity in the normal direction, as well [14]. Such regularity and orthogonality are not achievable with fully unstructured meshes, so it may be necessary to use prisms or other structured elements in conjunction with unstructured elements.

The third factor is design order of accuracy. In the presence of a shock, discretizations designed to be higher order accurate will be first order accurate. Subcell shock capturing may reduce the effort required for a specific result [45], but even so remains first order accurate. This first order error at shocks contaminates the solution globally, such that adaptive control (through h and/or p) is required to realize the advantages of discretizations with a high design order of accuracy. The global impact of errors at shocks is a particular concern for aeroacoustics [12, 13].

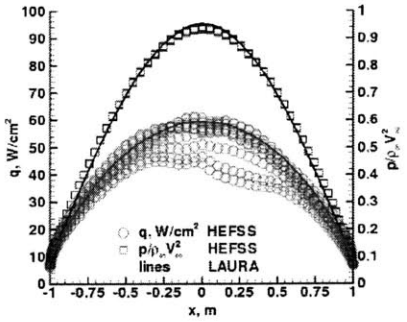

(a) Heat transfer and pressure coefficients. Different curves correspond to different span-wise locations.

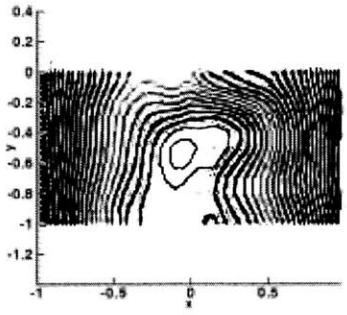

(b) Contours of heat transfer coefficient showing asymmetry in the stagnation region.

Figure 1-1: Heat transfer results from the High Energy Flow Solver Synthesis, reproduced from [26].

Some of these difficulties are captured in the results of a recent application aimed at predicting heat transfer on a cylinder. The method used was a 3D finite volume discretization with a high temperature gas model [24, 26]. A semi-unstructured grid of tetrahedra was used. It was produced by inserting diagonal faces into the hexahedra of a structured grid. The diagonals were biased uniformly in one direction in an attempt to force an incorrectly asymmetric solution. The tetrahedral mesh was used straight to the cylinder face, rather than utilizing prismatic or hexahedral cells in the boundary layer.

Figure 1-1(a) shows the results for pressure and heat transfer across the front half of the cylinder. There are ten curves for each quantity, one for each spanwise location, although the pressure curves are so well aligned that they appear as one. The heat transfer, on the other hand, shows significant spanwise asymmetry in the stagnation region. This is more apparent in the contour plot of heat transfer across the cylinder face, Figure 1-1(b). The magnitude of the asymmetry depended on the reconstruction algorithm used; the data displayed here were generated with the best reconstruction tested. Gnoffo suggests in [26] that a fully three-dimensional flux reconstruction would improve the results. He also suggests in [24] that stagnation region heating estimates may be susceptible to entropy gradients produced in the shock by mesh asymmetry. This example shows how sensitive heat transfer rates are to the shock capturing algorithm and the choice of flux and reconstructions.

1.4 Visualizing Higher Order Solutions

Most visualization software packages calculate the solution to be displayed at a generic point $(x,\ y,\ z)$ in an element by linearly interpolating the solution given at the element's nodes. Even most software-hardware interfaces, such as OpenGL [44], are configured to deal with linear display components. For piece-wise linear solutions, a linear display can be exact. For solutions described by highly curved, higher order polynomials, however – particularly those across shocks and boundary layers – the linear approximation may be very inaccurate.

The cost of inaccurate display is more than aesthetic. Depending on the magnitude of the display errors, bad display can prompt one to false conclusions about stalled solutions, about the numerical behavior of a simulation, or even about the physics of a problem. The types of display errors most frequently encountered with linear displays are cataloged by Buning in [10]. They include asymmetry of contour lines even on symmetric solutions, incorrect streamlines resulting from the accumulation of integration errors, and orientation-dependent (rather than solution dependent) shading within elements. A reliable visualization package is essential as a user interface with CFD. A standard, unimproved linear display is inadequate for higher order DG.

There are primarily two ways to improve the accuracy of a display for higher order interpolated solutions. The first, pixel-exact rendering, lights each pixel according to the solution at the pixel's coordinates. This is used in [69] to follow higher order space-time DG solutions by producing high quality videos. It has also been implemented with a modified version of OpenGL for cutplanes through DG solutions in [9]. As the results show, pixel-exact rendering produces remarkably clear displays. It tends to be on the slow side, however; [69] achieves ten frames per second, and this is apparently with heavy emphasis placed on observation rather than interactive probing. Visualization elements that are fully higher order have been developed in [67], which also references work on higher order hexahedra, higher order iso-surfaces (contours), and quadratic triangles. These are not strictly pixel-exact methods, although they are exact for polynomial solutions up to the order of the display element. They were designed for use with hierarchical data reduction methods, which enable small workstations to view results so large they are computed and stored on supercomputers. In this setting, higher order elements actually have a competitive advantage

in speed. They are much more efficient for transferring data between computers [67]. For individual workstation rendering, however, they remain slower than linear elements.

The second method, linear subdivision, or polygonization, breaks each computational element into a number of smaller, linear display elements. As the number of display elements increases, the accuracy of the linear representation also increases. An error-based polygonization algorithm is used to generate hierarchical surface meshes of 3D objects in [60]. Polygonization does not achieve the level of accuracy of a pixel-exact method, but it is fast.

Speed is an important consideration. The observations reported in [28] indicate that the largest part of a user's visualization time is spent probing and sampling flow field data. These operations are slowed as the number of nodes increases. With too many nodes, interactivity is reduced to a crawl. This can be just as crippling as an erroneous display. For example, when a user must make mouse movements slowly so as not to overshoot the desired cursor position, it quickly becomes tedious or impossible to extract data. Additionally, the lag time is wasteful and disruptive to concentration.

The issue of speed with fully higher order visualization elements and pixel-exact methods is not yet resolved. For this reason, the effort to improve the results of DG displays are directed at better polygonization. The most straightforward way to make improvements is to insert more linear subdivisions wherever the solution is not well approximated by the current linear representation. The idea of display error estimation is the same as that of [67], although the emphasis is on minimizing error rather than reducing data. Further discussion of this topic is deferred until Chapter 4.

1.5 Contributions of this Thesis

The key result is a demonstration that a higher order DG discretization can be used to simulate heat transfer in hypersonic flows with strong shocks.

Additionally, an error-based polygonization algorithm is implemented and demonstrated to improve the efficiency of displaying higher order DG solutions while maintaining display accuracy.

Chapter 2

Discontinuous Galerkin Method

2.1 Discretization of Navier-Stokes Equations

Following [43], the compressible, two-dimensional Navier-Stokes equations to model fluid motion can be written in strong conservation form as

$$\mathbf{u}_t + \nabla \cdot \mathcal{F}_i(\mathbf{u}) - \nabla \cdot \mathcal{F}_v(\mathbf{u}, \nabla \mathbf{u}) = 0, \tag{2.1}$$

where $\mathbf{u}$ is the conservative state vector,

$$\mathbf{u} = \begin{pmatrix} \rho & \rho u & \rho v & \rho E \end{pmatrix}^T, \tag{2.2}$$

$\mathcal{F}_i = (\mathbf{F}_i^x,\ \mathbf{F}_i^y)$ is the inviscid flux vector,

$$\mathbf{F}_i^x = \begin{pmatrix} \rho u \\ \rho u^2 + p \\ \rho uv \\ \rho uH \end{pmatrix}, \qquad \mathbf{F}_i^y = \begin{pmatrix} \rho v \\ \rho uv \\ \rho v^2 + p \\ \rho vH \end{pmatrix},$$

ρ is the fluid density, u and v are the components of velocity in the x and y directions, respectively, p is the pressure, $H = E + p/\rho$ is the total enthalpy,

$\mathcal{F}_v = (\mathbf{F}_v^x,\ \mathbf{F}_v^y)$ is the viscous flux vector,

$$\mathbf{F}_v^x = \begin{pmatrix} 0 \\ \frac{2}{3}\mu\left(2\frac{\partial u}{\partial x} - \frac{\partial v}{\partial y}\right) \\ \mu\left(\frac{\partial u}{\partial y} - \frac{\partial v}{\partial x}\right) \\ \frac{2}{3}\mu\left(2\frac{\partial u}{\partial x} - \frac{\partial v}{\partial y}\right)u + \mu\left(\frac{\partial u}{\partial y} + \frac{\partial v}{\partial x}\right)v + \kappa\frac{\partial T}{\partial x} \end{pmatrix},$$

$$\mathbf{F}_v^y = \begin{pmatrix} 0 \\ \mu\left(\frac{\partial u}{\partial y} - \frac{\partial v}{\partial x}\right) \\ \frac{2}{3}\mu\left(2\frac{\partial v}{\partial y} - \frac{\partial u}{\partial x}\right) \\ \frac{2}{3}\mu\left(2\frac{\partial v}{\partial y} - \frac{\partial u}{\partial x}\right)v + \mu\left(\frac{\partial u}{\partial y} + \frac{\partial v}{\partial x}\right)u + \kappa\frac{\partial T}{\partial y} \end{pmatrix},$$

μ is the dynamic viscosity, and κ is the thermal conductivity. The viscosity is calculated using Sutherland's Law, and $\kappa = c_p\mu/\mathrm{Pr}$, where Pr is the gas Prandtl number and c_p is the specific heat at constant pressure.

These constitute four equations in five unknowns. The fifth required relationship is the ideal gas equation of state, which when written in terms of the conserved quantities takes the form

$$p = \rho(\gamma - 1)\left(E - \frac{(u^2 + v^2)}{2}\right),$$

where γ is the ratio of specific heats.

The discretization of these equations is described in more detail in [21] and developed fully in [43]. It proceeds from this strong form through the weak form and into the discrete discontinuous Galerkin form. The viscous fluxes are discretized following the second Bassi and Rebay scheme [5, 6].

2.2 Newton Solver

The system is discretized in time with the backwards Euler method, and the spatial residual is linearized with respect to the current state vector. This yields a linear system for the state update, ΔU,

$$\left(\frac{1}{\Delta t}\mathcal{M} + \frac{\partial \mathbf{R}}{\partial \mathbf{U}}\right)\Delta \mathbf{U} = -\mathbf{R}(\mathbf{U}), \tag{2.3}$$

where $\mathcal{M}$ is the Mass matrix and $\mathbf{R}$ is the spatial residual. The solution is marched in time with Δt initially small to overcome transients and increased as the solution converges. The linear system is solved with the aid of a preconditioned GMRES method [55]. The preconditioner is the line solver described by Fidkowski, et. al. [21].

The solver, as well as the discretized form of the equations, are part of a discontinuous Galerkin package currently being developed at the Aerospace Computational Design Laboratory in the Department of Aeronautics and Astronautics at MIT [35].

2.3 Shock Capturing

The shocks that characterize supersonic flows of interest contain high frequency modes. These modes may be dispersed by spatial discretizations that would be higher order accurate on smooth, well-behaved problems[1]. The cause of this dispersion can be made clear through examination of the *modified* partial differential equation, examples of which are given in [3, 38] for the one-dimensional scalar advection equation. For higher Mach shocks these dispersed waves appear as oscillations strong enough to prevent a solver from converging to a stable solution. Special consideration is therefore required to simulate shocks with higher order methods.[2]

There are two primary categories of shock simulation. The technique of "shock fitting" is the most physically intuitive. The shock itself is treated as a computational boundary, and the analytic Rankine-Hugoniot relations are used to link both sides of the shock [40][3]. Its disadvantage is its complexity to code for general shock shapes and motions, which are not known in advance and must be calculated along with the solution.

The technique of "shock capturing" aims to allow stable shocks to arise without special consideration given to their movement and position. In the following section, previous work in shock capturing is reviewed.

[1]By practice and definition, the presence of the shock prevents these discretizations from being simply termed "higher order accurate discretizations." For brevity, the behavior of such discretizations on smooth problems may be refered to as "design order of accuracy," with a reference to this footnote.

[2]The subsequent subsections are derived from and anticipate the publication of the detailed work of Garrett Barter, who is responsible for the shock capturing method used in this work.

[3]This was the method employed by Moretti and Abbett for the first blunt body calculation [41].

2.3.1 Previous Work

The first class of capturing methods was proposed by von Neumann [64]. The governing partial differential equations are modified by the addition of a correction term that acts as viscosity would, smearing dispersive discontinuities into non-dispersive regions of merely large gradient. Besides smearing discontinuities, the artificial viscosity must meet three requirements. First, it must scale like the resolution of a discretization, such that as the resolution is increased the artificial viscosity can become arbitrarily small. Second, it must be proportional to some indicator of the discontinuity, such that in smooth regions its effect is negligible. Third, the Rankine-Hugoniot relations must still hold across the shock.

The second, more recent, class of capturing methods relies on the non-dispersive effects of discretizations designed for first order accuracy[4]. In regions near shocks, the discretization designed for higher order accuracy that is used elsewhere in the computation is replaced with one designed to be only first order accurate or some hybrid between the two. The replacement occurs typically in the numerical fluxes used, called "flux limiting" [8, 54], or in the slopes of state variables, called "slope limiting" [56, 57, 58].

Limiting methods are currently used for explicit DG solvers on unsteady problems [11, 17, 34, 46, 47]. While the use of limiters can prevent oscillations, a trade-off exists between monotonicity and convergence [62]. When the limiters are given a continuously differentiable form, such that they eventually settle at fixed values throughout the flow, the solution converges, but the shocks are no longer monotone. For an implicit, steady-state solution, convergence is required, but shock monotonicity would be desirable, as well.

There is a more subtle uncertainty about limiting that makes it not readily adaptable to higher order, implicit DG. When a solution is limited, the degrees of freedom are reduced. In order to prevent the problem from becoming over-constrained, the constraints must be reduced as well. The type of procedure required might be a continuously differentiable reworking of the discrete jump from $p = 1$ to $p = 0$ described in [17][5]. It is not clear how best to accomplish this.

[4] See footnote 1.

[5] Hereafter p is the solution polynomial order.

2.3.2 Higher Order Artificial Viscosity

Recently the artificial viscosity method has been applied to a higher order DG method by Persson and Peraire to capture one-dimensional Mach 10 and two-dimensional Mach 5 shocks [45]. It satisfies the original von Neumann requirements, which give it one further advantage. For a piecewise polynomial approximation, the resolution of a discretization scales like h/p. The required artificial viscosity is thus $\mathcal{O}(h/p)$, and it is possible to capture shocks with subcell resolution, rather than smearing them over several cells.

In the Laplacian form of the Persson and Peraire implementation, the artificial viscosity is applied as an additional term in the Euler equations,

$$\mathbf{u}_t + \nabla \cdot \mathcal{F}_i(\mathbf{u}) = \nabla \cdot (\epsilon \nabla \mathbf{u}). \tag{2.4}$$

The same approach is used here.

2.3.3 Entropy Residual and Viscosity Model

The Navier-Stokes equations with Laplacian artificial viscosity are written as

$$\mathbf{u}_t + \nabla \cdot \mathcal{F}_i(\mathbf{u}) - \nabla \cdot \mathcal{F}_v(\mathbf{u}, \nabla \mathbf{u}) = \nabla \cdot (\epsilon \nabla \mathbf{u}). \tag{2.5}$$

The implementation for this work differs from either the original von Neumann approach or the Persson and Peraire approach in the way it identifies elements near shocks. Whereas von Neumann used the gradient of a solution as a shock indicator, and Persson and Peraire used resolution differences between solution orders, the present method indicates a shock element by evaluating the production of entropy in that element. The exact entropy indicator is formulated below.

By the definition of entropy,

$$ds \equiv \frac{dQ_{\text{rev}}}{T}, \tag{2.6}$$

the entropy of a fluid particle undergoing a reversible, adiabatic process is constant,

$$\frac{Ds}{Dt} = 0, \tag{2.7}$$

or, considering a fixed point in space,

$$\frac{Ds}{Dt} = \frac{\partial s}{\partial t} + \vec{v} \cdot \nabla s = 0. \tag{2.8}$$

For steady flow without dissipative effects, $\vec{v} \cdot \nabla s = 0$ at every point in the flow field except in a shock. For an element, e, containing a shock, the average entropy generation is detected with the L_1 integral over that element. The normalized L_1 *entropy residual* for an element is thus defined as

$$R_{S,e} = \frac{k}{\delta} \int_e \psi(\vec{v} \cdot \nabla s) dA = 0, \tag{2.9}$$

where

$$\delta = \frac{1}{h} \int_e \lambda s dA \tag{2.10}$$

non-dimensionalizes the integral, $\lambda = u + c$ is the maximum characteristic wave speed calculated from quantities averaged over the element, c is the speed of sound, A is the element area, k is a gain factor, and $h = 4A/P$ is a characteristic length, where P is the element perimeter. The function ψ is the absolute value function modified to remove the discontinuity in the derivative, which would hinder convergence of the implicit solver.

$$\psi(x) \equiv \frac{x^2}{|x| + \varepsilon}, \tag{2.11}$$

where ε is a constant $\mathcal{O}(0.1)$.

The artificial viscosity, ϵ, to be applied to each element is directly proportional to the entropy residual,

$$\epsilon_e = \lambda \frac{h}{p} \frac{R_{S,e}}{\hat{R}_S}, \tag{2.12}$$

where p is the solution order, and $\hat{R}_S$ is an expected entropy change,

$$\hat{R}_S = \frac{s_2 - s_1}{\frac{1}{2}(s_1 + s_2)}. \tag{2.13}$$

The subscripts 1 and 2 refer to positions before and after, respectively, a normal shock at the average inflow Mach number. The expected entropy change is introduced to offset the magnitude of $R_{S,e}$, which is observed to be very large for strong shocks.

Even with the above normalization by $\hat{R}_S$, the amount of artificial viscosity added can be

extremely high at strong shocks. To limit the artificial viscosity, $R_{S,e}/\hat{R}_S$ is passed through a smooth minimum function, $x_{\min} = min(x, C)$, defined as:

$$x_{\min} = \begin{cases} C - \frac{1}{a}\log(1 + \exp(-a(x - C))) & \text{if } x_{\min} \geq 0 \\ 0 & \text{if } x_{\min} < 0, \end{cases} \tag{2.14}$$

where $a \geq 0$ is a smoothing constant. This form approximates the original min function well for $a = \mathcal{O}(100)$. It also produces only positive output, but in doing so introduces a discontinuity in the derivative for any x that cause $y = 0$. Assuming $a = \mathcal{O}(100)$, $y = 0$ occurs for positive x only with $C < \mathcal{O}(1 \times 10^{-3})$. The discontinuity can thus be avoided in practice. The capping values used with this function are given with the results.

Currently this entropy indicator is implemented for inviscid flow only. It has been used for viscous heat transfer calculations by applying it only outside the boundary layers. Viscous terms unrelated to shocks could be calculated with element viscous fluxes and removed from the entropy residual, making it of general utility.

Chapter 3

Discontinuous Galerkin Results

The DG method is compared against a hypersonic benchmark published by the NASA laboratory at Langley. Two finite volume codes were used for the benchmark, one structured and one unstructured. The first is the *Langley Aerothermodynamic Upwind Relaxation Algorithm* (LAURA). The second is the *Fully Unstructured Navier-Stokes* (FUN2D) code.

3.1 Description of Problem

The test case to be matched is the flow field around a right circular cylinder in a hypersonic flow [15, 25]. The free-stream conditions are given in Table 3.1. The Reynolds number is based on radius.

The publication of the original test case makes no mention of gas Prandtl number or thermal conductivity. It is assumed that the gas Prandtl number is constant, $Pr = 0.71$. Futhermore, the original test case did not specify whether viscosity was held at a constant value consistent with the given Reynolds number or adjusted as a function of state. It is assumed that the viscosity follows the Sutherland's law dependence on temperature[1,2].

Table 3.1: Test Case Flow Conditions

	Value
V_∞	5000 m/s
ρ_∞	0.001 kg/m^3
T_∞	200 K
M_∞	17.605
Re	376,930
γ	1.4
Pr	0.71
T_{wall}	500 K

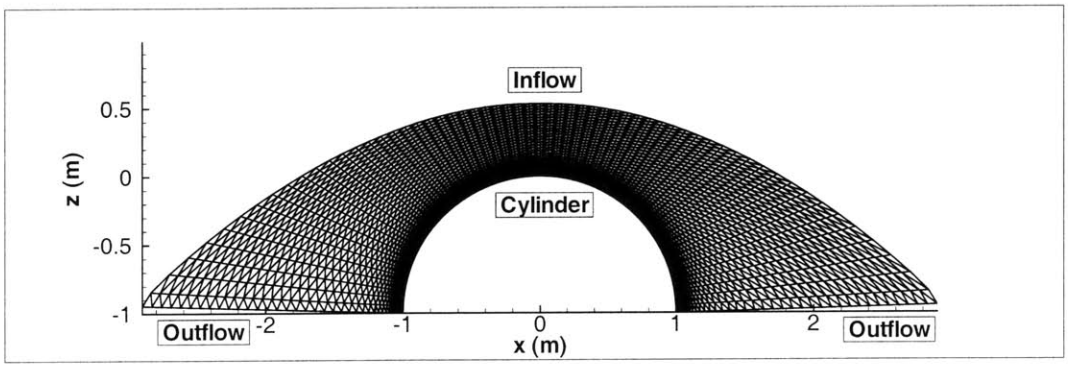

Figure 3-1: The computational grid.

3.1.1 Grid

The computational grid developed for the benchmark by Langley is shown in Figure 3-1. It is formed by creating a structured quadrilateral mesh around a cylinder of radius 1 m and cutting the quadrilaterals into triangles so as to uniformly bias the direction of the diagonals. This asymmetry makes for a difficult test case, as it may result in falsely asymmetric solutions. The computational domain is sufficiently large and refined to allow for resolution of both the detached bow shock and the viscous boundary layer using the LAURA code. Nodes near the inflow boundary have been aligned with the shock by means of the LAURA "align-shock option." The grid is 65 nodes normal to the body by 61 nodes circumferentially.

3.1.2 Boundary Conditions

As described in Section 2.1, the gas is modeled as thermally and calorically perfect. The free-stream is uniform and directed in the $-z$-direction. The cylinder surface is a "no slip" boundary at a constant temperature of $T_{\text{wall}} = 500$ K. Where the flow moves past either side of the cylinder and exits the computational domain, the FUN2D code uses an extrapolation boundary condition. The LAURA exit condition here is not specified but is presumed to be the same.

3.1.3 Langley Solution Techniques

Both Langley solutions were initialized to free-stream conditions. For robustness each solution proceeded in two steps. The FUN2D code was initially run with first-order accurate fluxes and after some iterations was run with second-order accurate fluxes. Convergence was determined by skin friction rather than the L_2 error norm, which was observed to stall. The LAURA code was first run with point-implicit relaxation and after some iterations was run with line-implicit relaxation.

[1]The close match of the presented results (below) with those already published, and the disparity between constant viscosity results and those published, appears to support this assumption.

[2]Sutherland's law is physically accurate for much of the boundary layer, and certainly for the thin, cooled region near the body [52].

3.2 Discontinuous Galerkin Results

3.2.1 Grid

The DG method is applied with three different grids. The first is the exact Langley grid with a linear representation of the cylinder surface, $q = 1$. The second is basically the same but with a quadratic, $q = 2$, description of the cylinder surface[3]. The higher order geometry is used following the observations of Bassi and Rebay, which suggest that superparametric elements are required with DG [4]. The third grid keeps the first 40 rows of elements in the boundary layer, but replaces the elements across the shock with badly aligned, fully unstructured elements. This grid will be refered to as the "partially unstructured" grid. Portions of both the structured and partially unstructured grids are shown in Figure 3-2 for comparison. The partially unstructured grid contains 60% more nodes than the structured grid; the primary purpose is to test the effect of shock-aligned elements on downstream flow properties.

3.2.2 Boundary Conditions

The exact Langley boundary conditions are matched. From the parameters given in Table 3.1 the full state vector, Equation (2.2), is calculated and specified along the inflow boundary (Figure 3-1). The cylinder surface is modeled with a "no slip" condition and a constant wall temperature of 500 K. At the outflow boundaries an extrapolation boundary condition is applied. The inviscid fluxes are calculated using state data from the interior of the grid. The three viscous boundary terms in the Bassi and Rebay 2 discretization for the artificial viscosity are set to zero because there is no artificial viscosity associated with the boundaries [5, 6]. Although the inviscid extrapolation boundary condition is observed to be generally unstable when the exiting flow is subsonic, the boundary layers do not cause stability problems except for low Re initial transients (see Section 6.1.2 on initialization).

[3]The $q = 2$ geometry is actually used to describe every element in the grid. See Section 6.1.2 on grid generation.

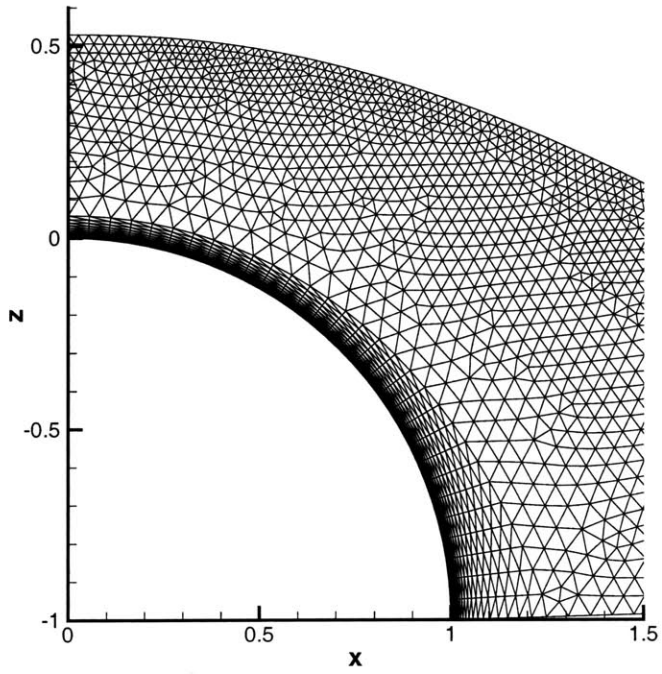

(a) The partially unstructured grid, with elements misaligned with the shock.

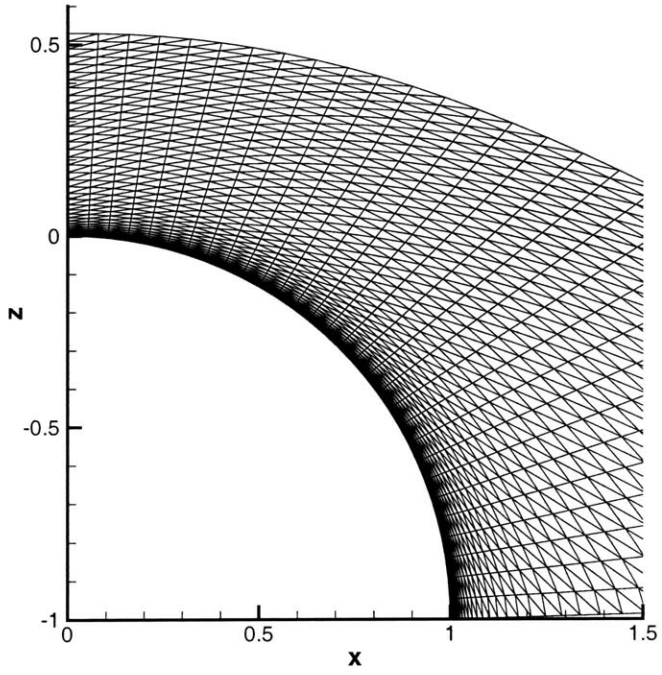

(b) The original structured grid

Figure 3-2: Close-ups of the grids

3.2.3 Solution Technique

The present DG method cannot converge a piecewise linear or higher ($p \geq 1$) solution when the flow field is initialized to free-stream conditions because a strong shock forms along the body and oscillations around the shock grow without bound. This is observed regardless of the amount of artificial viscosity added with the artificial viscosity model (Section 2.3.3). These oscillations are at first not visible in the conserved state vector quantities themselves, which when viewed independently appear to be normal. Rather, they first appear in combinations of conserved variables. For instance, pressure, (2.1), approaches zero, and Mach number increases by orders of magnitude. The problem is most often observed along the stagnation line, although with varied input and time stepping it can be made to occur in a number of places along the shock, usually symmetric with respect to the stagnation line. The present method can converge a piecewise constant ($p = 0$) solution from initialization at free-stream conditions. Nevertheless, a converged $p = 0$ solution cannot be used as a starting point for a $p = 1$ solution because the same instability returns. This again seems to be true regardless of attempts to stabilize the shock with the artificial viscosity model.

It may be possible to avoid either of these two difficulties with more careful consideration given to finding a stabilizing cap and gain (defined in Section 2.3.3). For this work, however, a two-step solution procedure was found to be the most robust. The first step is to solve an "easier" problem on the target grid, for example, $M = 10$, $Re = 10,000$, $p = 0$, initialized to free-stream conditions. The second step is to restart from this converged $p = 0$ solution while simultaneously increasing M, Re, and p. This establishes a transient $p = 1$ solution at the weaker, lower Mach shock, around which oscillations are manageable, before the higher Mach flow moves in from the boundary. From this converged $p = 1$ solution all higher order interpolations will converge at high Mach number.

The inviscid fluxes for these results are calculated using the Lax-Friedrichs flux. The Roe flux is observed to carbuncle at $p = 0$ [48]. The carbuncle cannot be used as an initial condition for a higher p solution with either flux. With a valid $p = 0$ solution, on the other hand, i.e., the Lax-Friedrichs solution, either flux can be used for higher p solutions. In the latter case, the Roe flux requires more artificial viscosity (results below). Unless otherwise noted, all data is presented for the Lax-Friedrichs flux.

3.2.4 The Overall Flow Field

Figures 3-3 show the entire flow field in a contour plot of non-dimensionalized pressure, which ranges from 0 to 0.9 over 18 contours in each subfigure. The DG second order accuracy result on the structured $q = 1$ grid is in good qualitative agreement with the Langley codes. The result is visibly identical on the structured $q = 2$ grid (not shown) and very similar on the partially unstructured $q = 1$ grid, Figure 3-3(c).

3.2.5 Line Plots Through the Shock

Figure 3-4 compares the solutions of each of the three codes in a plot of density ratios along the stagnation line[4]. The DG results here are shown with the design $\mathcal{O}(h^2)$ accurate discretization, $p = 1$, to match the design order of the FUN2D and LAURA discretizations[5]. The cylinder is at $z = 0$ m. The empirically determined cap and gain on the entropy indicator required to stabilize the shock, $C = 1.75$ and $k = 0.3$, (Section 2.3.3), were used for the $q = 1$ structured grid, and $C = 1.75$, $k = 0.4$ were used for the partially unstructured grid[6]. Three points are sampled in each element. The shock is smeared across approximately eight elements and appears monotone. The results are in good agreement with the Langley results.

Figure 3-5 examines the effect of increasing p on the resolution of the shock with the $q = 1$ structured grid, now displayed with 15 evenly distributed points per element. Both the $p = 1$ and $p = 4$ cases are run with the same gain on artificial viscosity, so as p increases, the artificial viscosity is reduced (Equation 2.12). The result is a visible sharpening of the shock at $p = 4$, for which the shock is smeared over only three elements. Although the $p = 4$ solution does not display the sub-cell shock capturing demonstrated by Persson and Peraire, they note a similar result for their Laplacian artificial viscosity method: it appears to result in wider shocks than the use of a model based on the physical dissipation of an ideal gas. The two methods are compared in [45].

[4]For all line plots, the Langley benchmark results displayed are the averages of the nearest cell centers.

[5]As mentioned previously, all discretizations are only $\mathcal{O}(h)$ with shocks.

[6]The density behind the shock is on average too low if $k = 0.4$ is used with the structured grid; this is because the shock is smeared too far forward. The difference in k is just a result of the order in which k was tried, it being adjusted only for unconverged or unsatisfactory solutions.

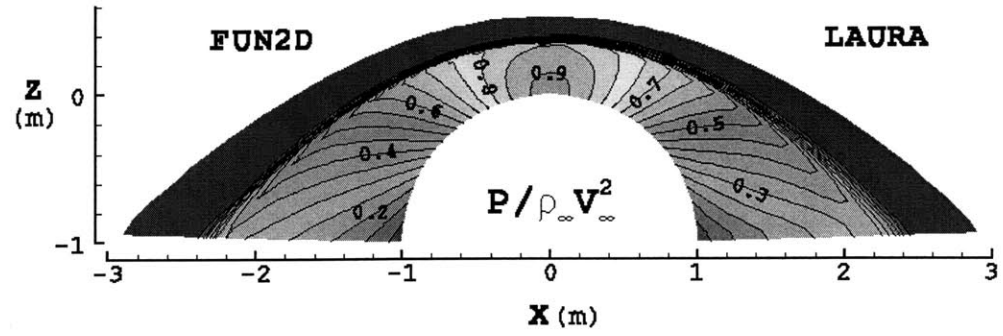

(a) Langley FUN2D and LAURA

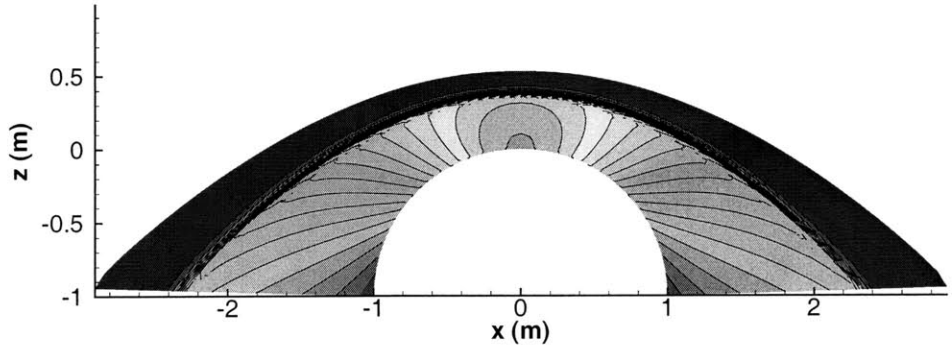

(b) Discontinuous Galerkin $p = 1$, $q = 1$ structured grid

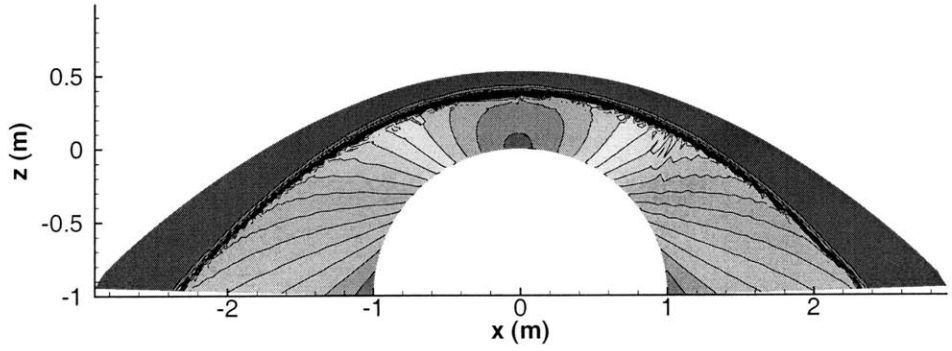

(c) Discontinuous Galerkin $p = 1$, $q = 1$ partially unstructured grid

Figure 3-3: Contours of non-dimensional pressure, $p/\rho_\infty V_\infty^2$, in 18 intervals from 0 to 0.9.

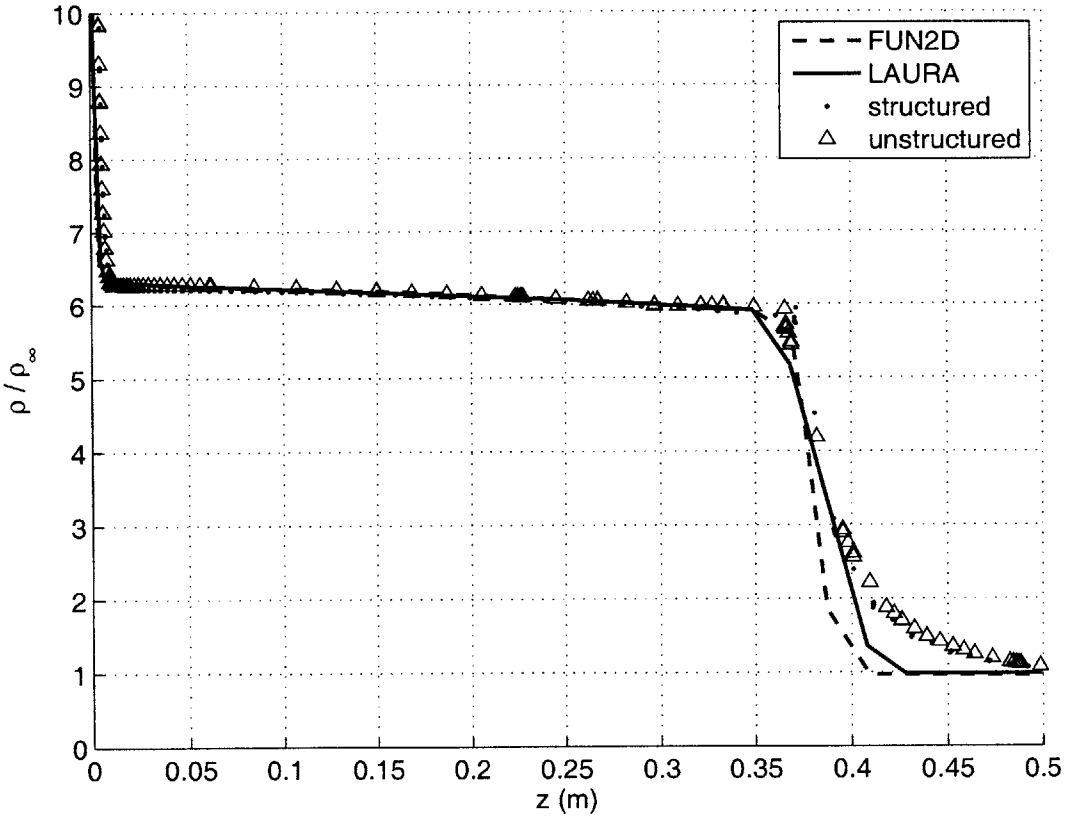

Figure 3-4: Density along stagnation streamline compared against benchmark. The solution is $p = 1$ on the $q = 1$ structured and partially unstructured grids.

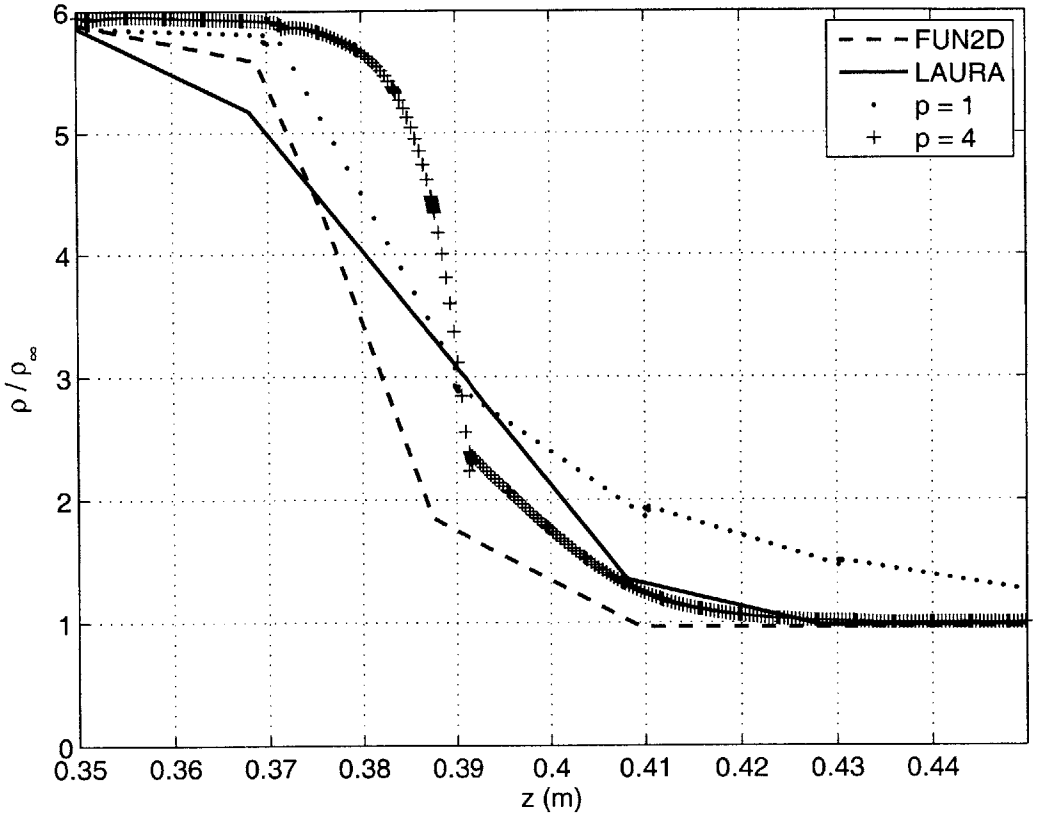

Figure 3-5: The effect of interpolation order on shock smearing. The grid used is the $q = 1$ structured grid.

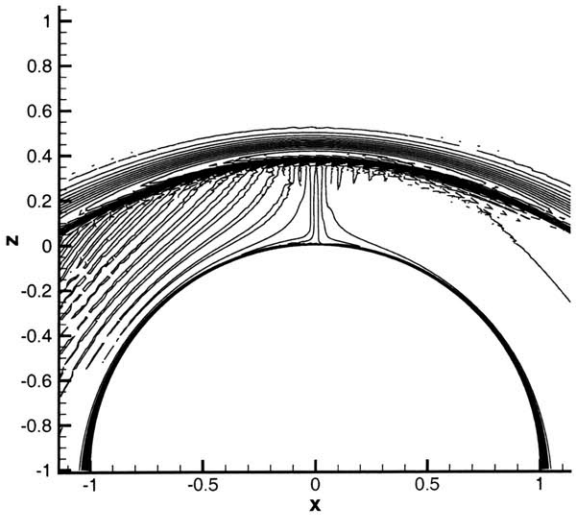

Figure 3-6: Stagnation temperature variation behind shock, $T_t/T_{t\infty}$, in 100 contours between 0.04 and 1.05; $p = 2$, $q = 1$ structured grid.

3.2.6 The Flow Behind the Shock

Figures 3-6 and 3-7 show contour plots of stagnation temperature behind the shock, with 100 intervals between the minimum and maximum flow field values. These are clearly asymmetric in both cases, with greater asymmetry at lower p.

Figures 3-8 show line plots of stagnation temperature, normalized by the free-stream value, from approximately (0.5, 0.2) to (−0.5, 0.2), which is a line behind the shock and perpendicular to the direction of the free-stream, for $p = 2$ and $p = 4$. The asymmetry is more pronounced for lower p. The graphs are clearly oscillatory, whereas the inflow conditions are not. These oscillations are larger with higher p. The results shown for $p = 4$ produced with cap and gain on the shock entropy indicator of $C = 1.75$ and $k = 0.4$ correspond to a peak artificial viscosity in the shock along the stagnation line of $\epsilon_e = 8 \times 10^{-3}$. Alternatively caps of $C = 2.75$ and $C = 1$ were tried, for peak artificial viscosities along the stagnation line of 11×10^{-3} and 4×10^{-3}. The magnitude of the largest oscillation is approximately 33% lower for $\epsilon_e = 8 \times 10^{-3}$ compared with $\epsilon_e = 4 \times 10^{-3}$, although the oscillations are the same size for $\epsilon_e = 4 \times 10^{-3}$ and $\epsilon_e = 11 \times 10^{-3}$, so no trend with artificial

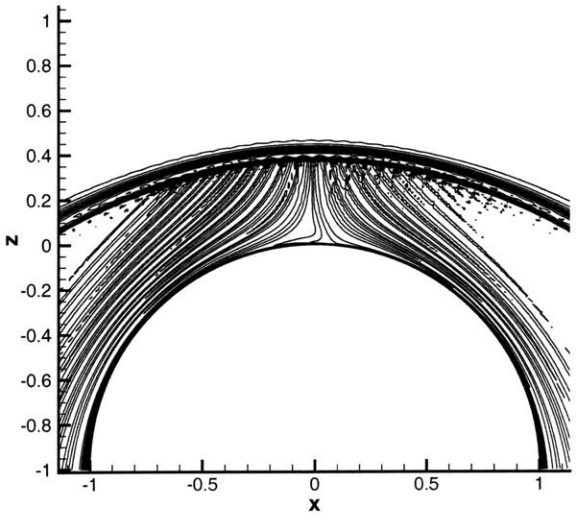

Figure 3-7: Stagnation temperature variation behind shock, $T_t/T_{t\infty}$, in 100 contours between 0.04 and 1.05; $p = 4$, $q = 1$ structured grid.

viscosity is apparent[7]. These oscillations may have an effect on the surface quantities (see below), which are also oscillatory, although causality is not clear; the region of these line probes is subsonic, so the oscillations could be caused by, rather than the cause of, something downstream. It seems most likely, however, that they are the result of oscillations in the captured shock.

3.2.7 Surface Plots

The $q = 1$ structured grid is considered first. Plots of surface pressure coefficient, heat transfer coefficient, and skin friction coefficient are shown for three different p in Figures 3-9, 3-10, and 3-11 as a function of angle measured from the stagnation line ($\theta > 0$ corresponds to $x > 0$)[8]. The LAURA pressure coefficient is very nearly the FUN2D pressure coefficient, so only one is shown.

The salient feature of these surface quantities is the discontinuous jump in the solution between each element. To some extent this is expected because DG allows for these jumps. The oscillations are also, to some extent, expected as a result of the linear geometry, which

[7]Time constraints prevented a more thorough investigation.

[8]$p = 4$ was also tested and is very similar to $p = 3$

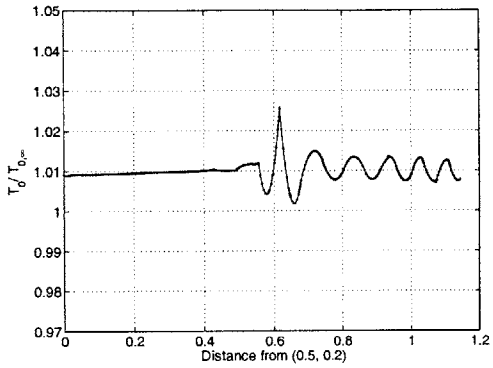

(a) Stagnation temperature line plot $p = 2$

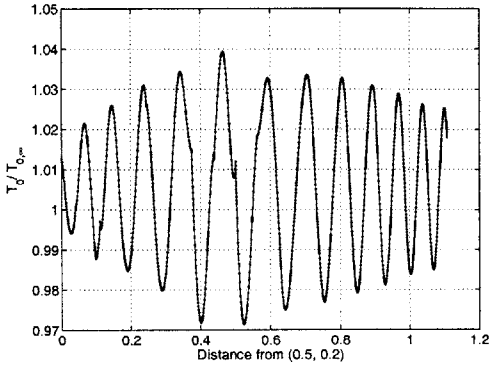

(b) Stagnation temperature line plot $p = 4$, $C = 2.75$

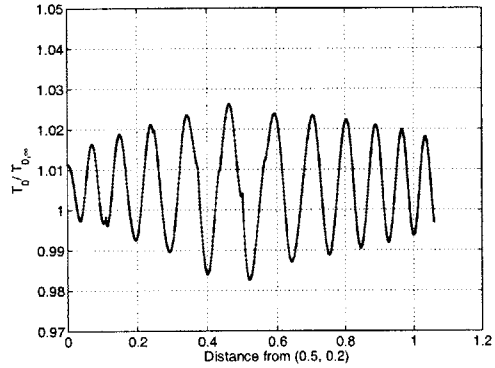

(c) Stagnation temperature line plot $p = 4$, $C = 1.75$

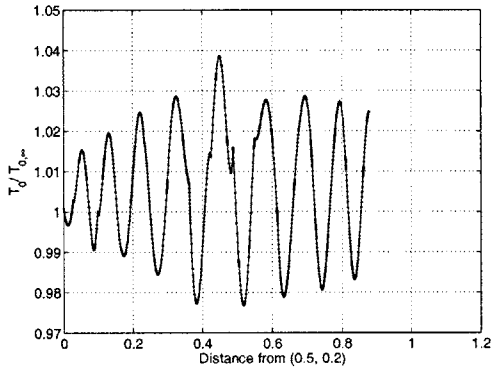

(d) Stagnation temperature line plot $p = 4$, $C = 1.0$

Figure 3-8: Stagnation temperature line plots behind the shock showing oscillations, $q = 1$ structured grid.

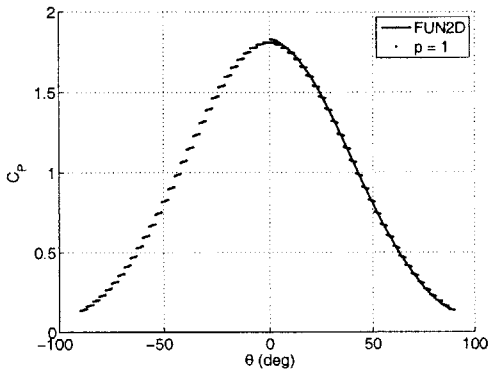

(a) C_P

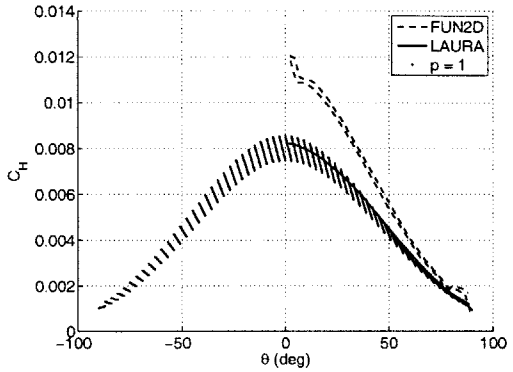

(b) C_H

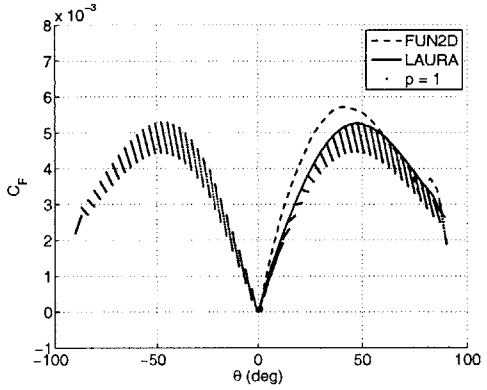

(c) C_F

Figure 3-9: Surface quantities, $p = 1$, $q = 1$ structured grid

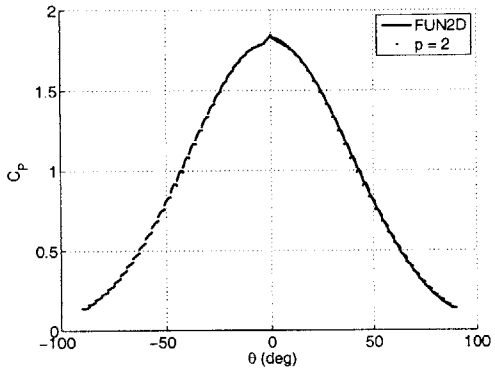

(a) C_P

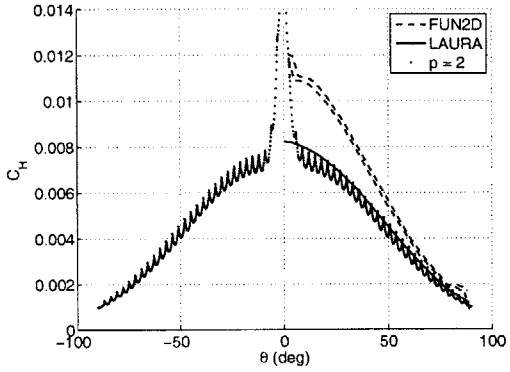

(b) C_H, spike reaches $\approx 1.75 \times 10^{-3}$

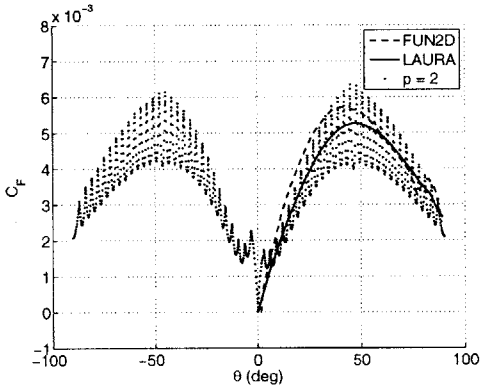

(c) C_F

Figure 3-10: Surface quantities, $p = 2$, $q = 1$ structured grid

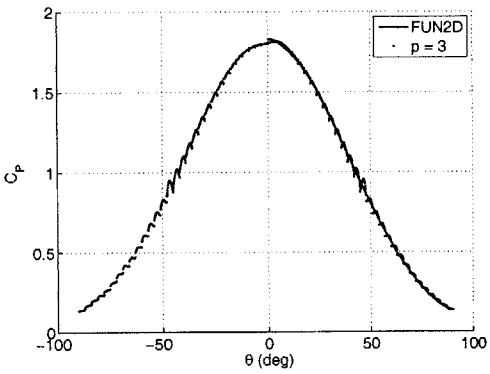

(a) C_P

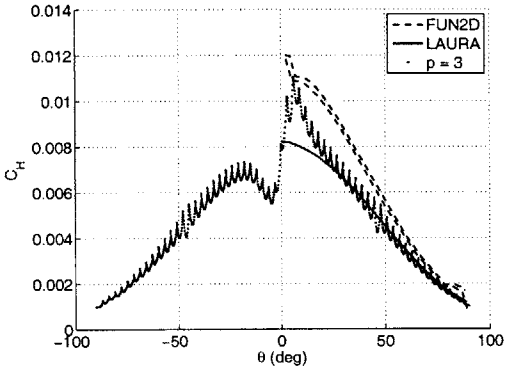

(b) C_H

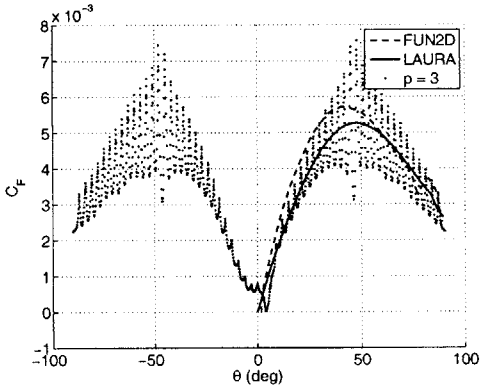

(c) C_F

Figure 3-11: Surface quantities, $p = 3$, $q = 1$ structured grid

introduces a radial error in the position of the cylinder face and discontinuities in the slope between faces. It is expected that for higher p, both the interelement jumps and oscillations will be reduced. This is observed with pressure, which quickly becomes consistent with the FUN2D line and the LAURA line (not shown, nearly the same as FUN2D), as well as with the modified Newtonian pressure coefficient [2]. For the skin friction, however, the oscillations are not reduced, but rather appear to worsen. For the heat transfer, the $p = 2$ solution is worse than the $p = 1$ solution, but $p = 3$ spikes less than $p = 2$.

The Roe flux was used to calculate a $p = 2$ solution on the same grid. Whereas the Lax-Friedrichs flux used a cap and gain as small as $C = 1.75$, $k = 0.4$, the Roe flux required more; values of $C = 5$, $k = 1.2$ were used, although no attempt was made to find the minimum required. The results, no better than the Lax-Friedrichs results, are shown in Figure 3-12.

Figure 3-13 shows the $p = 1$ solution on the $q = 1$ partially unstructured grid. The only significant difference between the input for this test and the $p = 1$ test on the $q = 1$ structured grid is the alignment of elements across the shock. Here they are not well aligned. Comparison of the two heat transfer graphs, Figure 3-13(b) and Figure 3-9(b), show that this makes a difference, of the order of the jumps between elements. This supports the suggestion made by Gnoffo in [24] that errors in the shock capturing caused by a poorly aligned grid can wash downstream and affect stagnation region heating estimates. This is the most plausible explanation for the difference, as the boundary layer gridding and simulation conditions are otherwise equal between this case and the structured one. Figure 3-14 shows $p = 2$ results on the same $q = 1$ unstructured grid. In this case, the unstructured results for heat transfer look better than the structured results. The results are similar for $p = 3$ (not shown).

Figure 3-15 shows the the $p = 2$ solution on a $q = 2$ grid, for which every element is described by higher order geometry, see Section 6.1.2, grid generation. Higher order geometry does not improve the solution to the extent that would be expected, except for the pressure curve, which is very smooth. The $q = 2$ geometry appears not to improve, however, the skin friction and heat transfer results. The conclusions drawn from these results are given in Section 6.1.

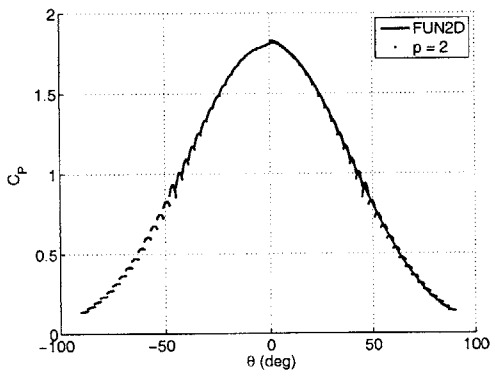

(a) C_P

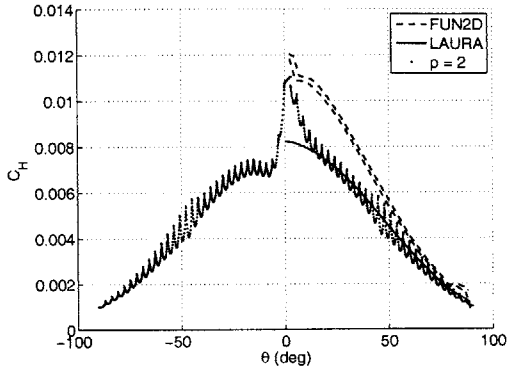

(b) C_H

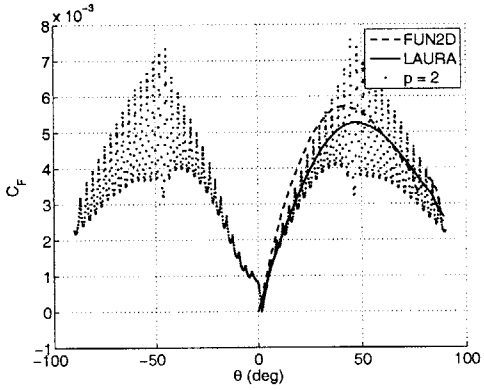

(c) C_F

Figure 3-12: Surface quantities, $p = 2$, $q = 1$ structured grid, with the Roe flux

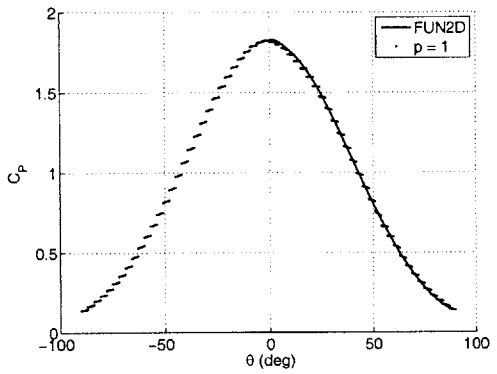

(a) C_P

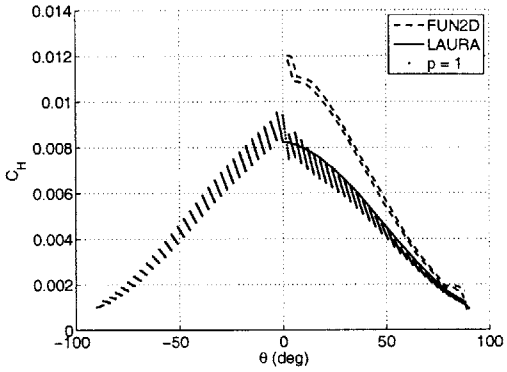

(b) C_H

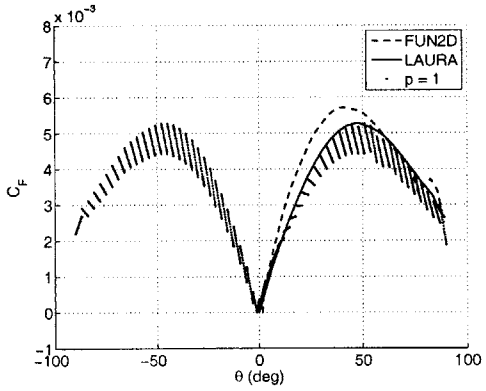

(c) C_F

Figure 3-13: Surface quantities, $p = 1$, $q = 1$ partially unstructured grid

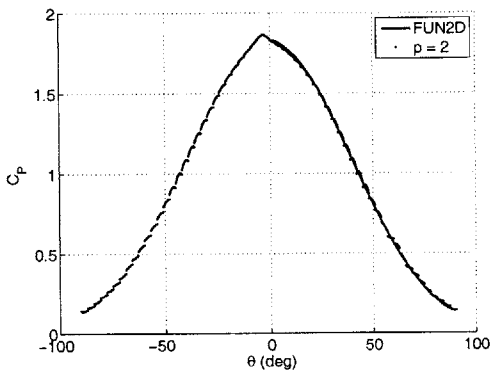

(a) C_P

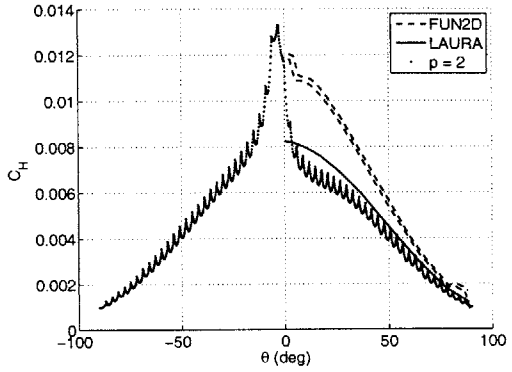

(b) C_H

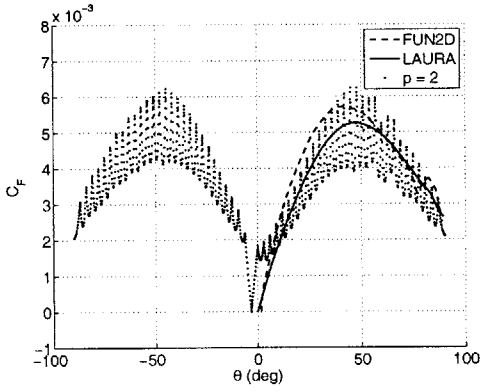

(c) C_F

Figure 3-14: Surface quantities, $p = 2$, $q = 1$ partially unstructured grid

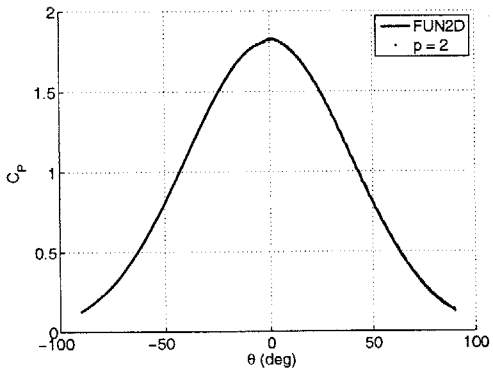

(a) C_P

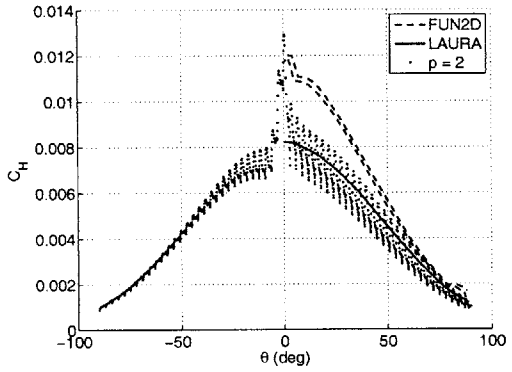

(b) C_H

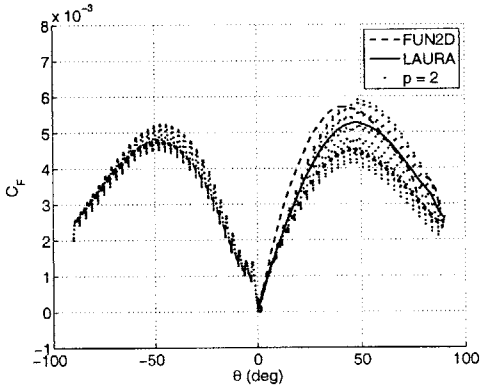

(c) C_F

Figure 3-15: Surface quantities, $p = 2$, $q = 2$ structured grid

Chapter 4

Visualization Method

4.1 Current Practice

The higher order interpolation solutions generated with this DG method are visualized with the Visual3 display package [28, 29, 30, 31]. Visual3 takes as input a list of grid node coordinates, connectivity data linking those nodes into elements, and solution data at each node. It displays a solution by linear Gouraud shading between nodes [27].

The accuracy of the linear approximation to the higher order solution is currently improved by uniform, isotropic[1] subdivision of each computational element into a number of smaller display elements. The number of subelements in the current method is n^d, where d is the problem dimensionality (2 or 3) and n is the larger of the solution interpolation order, p, or the geometry interpolation order, q. This method is simple to implement. A polynomial solution in any basis can be converted to the nodal Lagrange basis, which uses as its weights the solution at the nodes of an isotropic subdivision of p^d elements. For $q = 1$ elements, the Lagrange data is copied directly to Visual3. For $q > 1$ elements, the same number of points are sampled, n^d, but the points are evenly spaced over the curved element. Overall the procedure is simply a matter of sampling the solution at some points and copying the data to Visual3. But this method has two disadvantages. First, it provides no guarantee of display accuracy. Second, it introduces nodes independent of the quality of the display, resulting in additional nodes where the linear display was already adequate. This extra computational expense slows user interactivity with the visualization software.

[1] Or best approximation, for tetrahedra.

Consider the two-dimensional (2D) $M = 1.5$ flow over a diamond airfoil approximated by piece-wise fifth-order polynomials on a grid with 212 discontinuous elements. The minimum display grid has $636 = 212 \times 3$ nodes[2], Figure 4-1(a). Figure 4-1(b) shows contours of non-dimensional density, ρ/ρ_∞, with 10 contour levels in increments of 0.04 using the computational grid as the display grid. Figure 4-1(d) shows the same contours, but using the grid in which each computational element is isotropically subdivided into 25 display elements (Figure 4-1(c)).

The leading and trailing edge shocks are visible without subdivision, but the expansion fan is completely lost. On the other hand, the uniform isotropic subdivision correctly displays the expansion fan, but there are now $4452 = 212 \times 21$ nodes in the display grid (an increase of 700%). Approximately seventy of the computational elements are ahead of the leading shock, where the flow is uniform, so that approximately $1260 = 70 \times (21 - 3)$ nodes inserted above the minimum number required are not adding any new information to the display. This is more than a quarter of the nodes added for this problem.

The excess is compounded in 3D, as each computational element is subdivided into n^3 display elements. On an Intel Pentium 4, 2.53 GHz processor with 512 MB RAM it takes approximately 16 seconds to load a 3D grid with 50,000 $q = 1$ elements and a $p = 1$ solution, where no refinement is called for. More importantly than load time, the size of the display is sufficiently large to cause noticeable lag between action and response when probing the data.

The trade-off is between accuracy and efficiency. A more efficient way to display results would be to add points only when needed, and to keep adding points until the linearly displayed solution resembles the computed higher order solution to within some desired accuracy. This requires better preprocessing, but leaves intact the core of Visual3, which has proved itself to be a fast and reliable research tool. The first step in this preprocessing is accurately assessing the error in a display.

[2]A note on node counting: The nodes joining computational elements become different but overlapping display nodes for DG visualization because solution data is discontinuous across elements. The minimum number of display nodes for an unstructured DG grid is thus considered to be $n_e(d+1)$, where n_e is the number of elements. When additional nodes are inserted for the purpose of display, however, they connect subelements within a single computational element. Thus the solution data, and therefore nodes, are shared between subelements. For a $p = 5$ solution, isotropic subdivision results in 21 nodes per element.

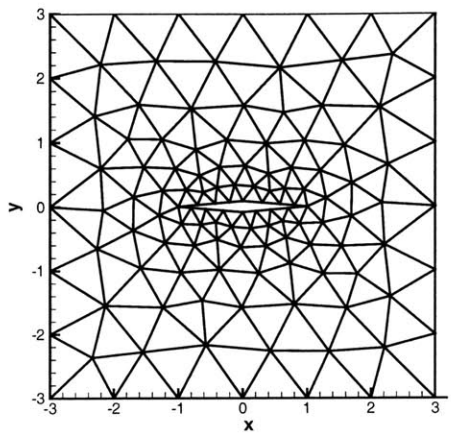

(a) Computational grid as display grid

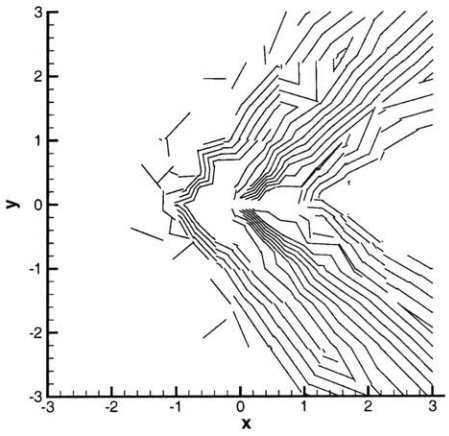

(b) Linear display on computational grid

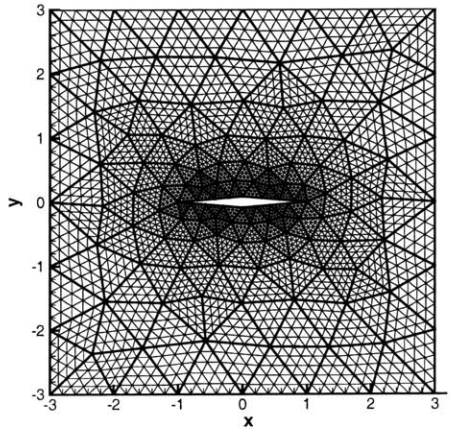

(c) Uniformly, isotropically refined display grid

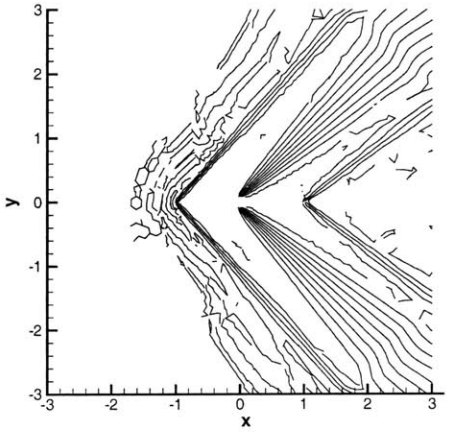

(d) Linear display on refined display grid

Figure 4-1: Uniform isotropic subdivision; contours are of ρ/ρ_∞ in 10 levels from 0.84 to 1.2

4.2 Estimating the Error in a Display

The error of a display depends on the magnitude of the difference between the higher order solution, u, and the linear interpolation between nodes, u_L. A standard norm that can be used to evaluate the error is

$$L_a(v) = ||v||_a = \left[\int_\Omega |v|^a d\Omega\right]^{1/a}, \tag{4.1}$$

where a is the measure of the norm and Ω can be the element edges l, faces f, or interiors i in a grid, and v is the function being measured. The norms used here are the L_1 and L_∞ of the display error,

$$||u - u_L||_1 = \int_\Omega |u - u_L| d\Omega,$$
$$||u - u_L||_\infty = \max_\Omega |u - u_L|.$$

Rather than calculate the L_∞ norm, it is approximated as

$$||u - u_L||_\infty \approx \max_c |u(x_c) - u_L(x_c)| = ||u - u_L||_\infty^c, \tag{4.2}$$

where x_c are a set of sampling points[3]. The set of sampling points, $\{c\}$, are chosen as the union of the sets of quadrature points on element interiors, $\{i\}$, edges, $\{l\}$, and faces (in 3D) that would exactly integrate the piecewise polynomial error of a conserved state variable[4]. This work considers only the 2D case and presents L_1-type error results for the grid interior only.

For consistent application of these global error estimates across different grids, they are

[3] An optimization problem might be solved to find the true L_∞ norm, although this has not been pursued for this work.

[4] Although combinations of state variables, such as Mach number and pressure, can be used as an error indicator, they will not in general be polynomial of the same degree as the solution order. This would affect the choice of quadrature rule used to approximate the integrals if a certain accuracy was desired.

non-dimensionalized:

$$E_1 = \frac{||u - u_L||_1}{||u||_1},$$
$$E_\infty = \frac{1}{||u||_1^{i_{\max}}/A^{i_{\max}}} \max_{\{l,i\}} |u - u_L|.$$

The local pointwise error used to direct node insertion (see below) is normalized by local quantities[5]. The global E_∞ estimate is non-dimensionalized in the same way to be consistent with the estimate controling node insertion; here $i_{\max}$ is the element in which this global error occurs, and $A^{i_{\max}}$ the area of this element. This non-dimensionalization will not be reliable if the average value of the state variable chosen is zero for an element. Alternatively, if a user cannot find a state variable that is, on average, never zero, the dimensional forms of the error estimates can be used.

The L_1 norm is approximated using a higher-order quadrature rule on the computational element. The solution basis, ϕ, for a computational element is polynomial of degree p in the physical space, even when the elements are curved. This is ensured by defining the solution basis on the linear *shadow reference element*, rather than on the physical element [21]. The shadow element is formed by connecting the vertices of the element with straight lines, see Figure 4-2, and its reference is a rotation and stretching of the shadow into convenient coordinates. To sample the solution at a physical point, x_c, its coordinates are mapped to the shadow reference space. The locations of x_c, however, are first mapped from locations, ξ_c, in a reference element, which in 2D has vertices $\{(0,0),(1,0),(0,1)\}$, because this is where the quadrature point locations are defined. Thus the discrete form of an area integral is

$$\int_e f(\phi) d\mathbf{x} = \sum_g w_g f(\phi(\mathbf{B}^{-1}\mathbf{A}(\xi_g)))|\mathbf{J}|, \tag{4.3}$$

where f is the function to be evaluated, ϕ are the basis functions on the shadow reference element, w_g is the weight of quadrature point g, $\mathbf{J}$ is the Jacobian of the mapping from the reference element to the physical element, and $\mathbf{A}$ and $\mathbf{B}^{-1}$ are the mappings between elements shown in Figure 4-2.

[5]This gives something closer to a pointwise percent error than normalization by $||u||_1$ over the entire grid.

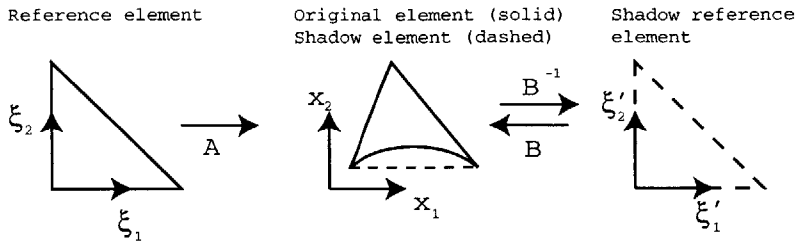

Figure 4-2: Reference and shadow elements for an original (computational) element. Reproduced, by permission, from [21].

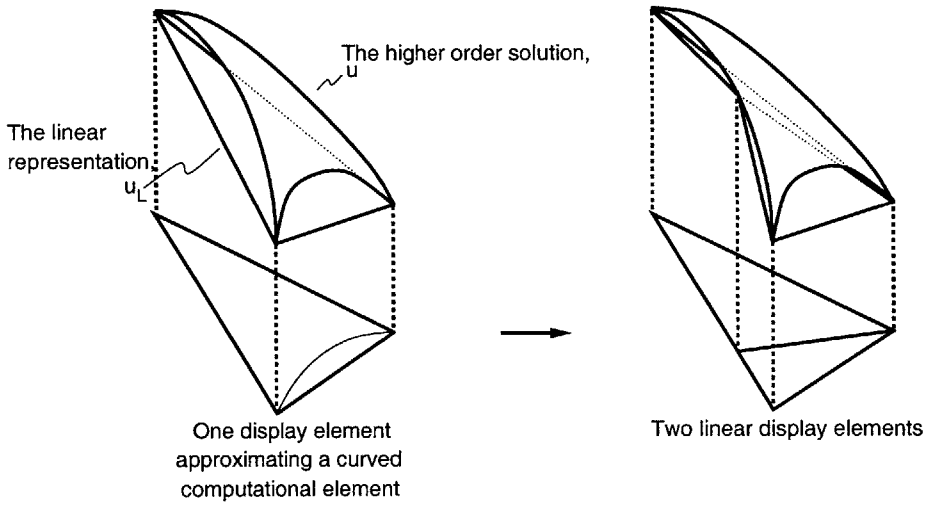

Figure 4-3: The addition of a display node. The location of the largest point-wise error in an element is the location of the next display node to be inserted.

4.3 Display Refinement

The refinement algorithm is called for each computational element, which is treated as an independent grid that may have its interior remeshed with linear display elements.

Consider an example of the process with a single, curved computational element, Figure 4-2, center. Initially, the display mesh consists of a single linear display element, which, except for the curved side, matches the computational element in space. The two are shown at left in Figure 4-3, with their solutions depicted elevated above them. The higher order solution is not well represented by the linear solution, which exactly represents the higher order solution only at the three display nodes.

The location of a new display node is taken to be the location, c, of the largest calculated

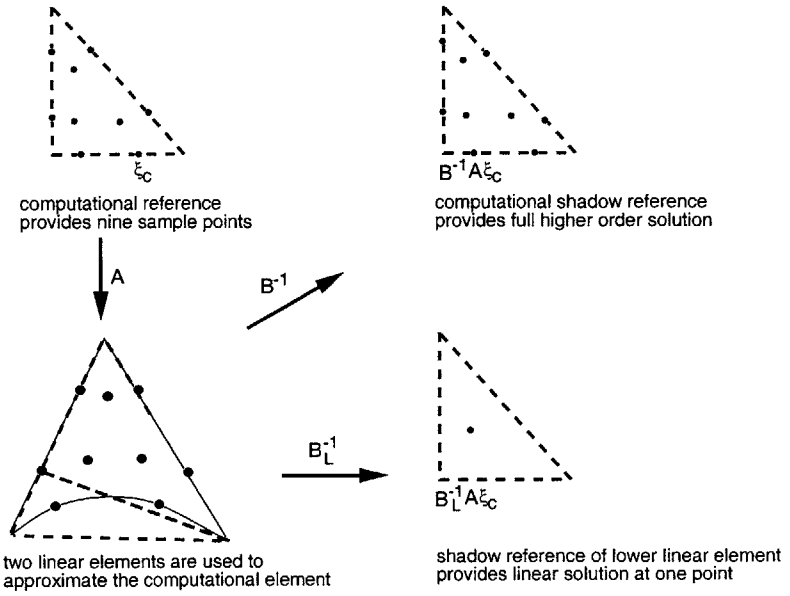

Figure 4-4: Points evaluated for error are fixed in the computational element. The linear elements encompassing any of these points may change.

point-wise error in a computational element, if this error is larger than some user-specified tolerance, E_{tol}. The algorithm effectively seeks to control the E_∞ error estimate element-by-element. The first step of inserting a display node is to evaluate the pointwise error,

$$E_c = \frac{1}{||u||_1/A}|u(x_c) - u_L(x_c)|$$

at each quadrature point c; here $||u||_1$ and A are for the element, not the grid. Assume for the purpose of illustration that one node has already been inserted in the display mesh for this computational element, as shown at the right of Figure 4-3, making two linear display elements. The same display mesh is shown at the lower left of Figure 4-4. The calculation of this error proceeds as follows, using the notation of the previous section. The quadrature point, c, has been defined on the computational *reference element* at position ξ_c (upper left of figure). Its physical location is $x_c = A(\xi_c)$. The higher order solution is defined on the computational *shadow reference element*, where it is sampled at point $B^{-1}A(\xi_c)$ (upper right). The higher order term of the pointwise error is, $u(x_c) = u(\phi(B^{-1}A(\xi_c)))$. This interpolation procedure is also the method by which $||u||_1$ is evaluated, following Equation (4.3).

The linear solution, u_L, is evaluated at the same physical point x_c. This first requires

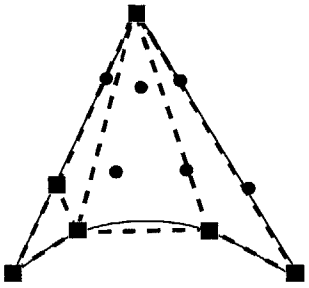

Figure 4-5: Approximation of a curved computational element. The display nodes for this figure are squares to differentiate them from the remaining quadrature points.

finding the linear element containing this point. It then requires calculating the location corresponding to x_c in the *display* shadow reference element, $B_L^{-1}x_c$. The linear basis ϕ_L is interpolated at this point. The second term of the pointwise error is, $u_L(x_c) = u(\phi_L(B_L^{-1}A(\xi_c)))$.

Note that the choice to select quadrature points on the computational element, rather than on each linear element, has two advantages. First, it allows the higher order solution and norm, u and $||u||_1$, to be sampled at the beginning of refinement and stored until refinement is complete, no matter how many linear display elements are created. In practice, sampling higher order solutions can be time consuming, and this keeps the burden to a minimum. Second, it automatically provides a way to respect curved element boundaries. Because the mapping from the reference element to the computational element includes the non-linear effects required to get the shape of the curved element, every quadrature point inside (or on the edge of) the reference element is guaranteed to correspond to a point inside (or on the edge of) the physical element.

The result of further hypothetical refinement is shown in Figure 4-5. There are now six display nodes, which include the original element vertices. The curved geometry is now beginning to show through.

The entire algorithm is summarized in three functions below.

RefineElement(j)

1. Obtain quadrature points, $\{c\}$, for interior and edges in computational element, j, according to the solution or geometry order, whichever is larger.

2. Interpolate higher order solution to $\{c\}$.

3. While bad quadrature points remain:

   - For each c:

     Call CheckPoint(c) to find E_c.

     If $E_c > E_{\text{tol}}$ Then count c as a bad point.

     If $E_c > E_{\text{tol}}$ and $E_c > E_{\text{worst}}$, Then $c_{\text{worst}} = c$ and $E_{\text{worst}} = E_c$.

   - If there are bad points Then Call InsertNode(c_{worst}).

The algorithm loops until either all points c are below the error tolerance or a node has been inserted at each quadrature point[6]. To save time, once a node has been inserted at c that point is not checked again, as the error will be zero. On the other hand, points that do not yet have nodes inserted at them are rechecked after each remeshing, even if previously they were considered "good." This is because the remeshing that follows node insertion can change the subelement containing a point c, thereby changing the error at c.

The two functions used by the algorithm are described below.

CheckPoint(c)

1. Locate the subelement containing c.

2. Linearly interpolate from the subelement nodes to c to get the linear solution at c.

3. Calculate E_c.

Locating the subelement containing c is accomplished by testing, for each edge in a subelement, whether c is on the same side of the edge as the third vertex in that subelement. In general, for a convex polygon with consecutive, non-colinear vertices $\{X_1 \ldots X_N\}$, where $N \geq 3$, the point c will be inside of edge j, which links vertices X_j and X_{j+1}, if $(\overrightarrow{X_jX_{j+1}} \times \overrightarrow{X_jc}) \cdot (\overrightarrow{X_jX_{j+1}} \times \overrightarrow{X_jX_{j+2}}) > 0$. See Figure 4-6. Thus if the test is negative for any edge in a polygon, c is not in that polygon. This test is not reliable when c is on an edge of the computational element (especially if the edge is curved). In this case the test is unnecessary, however, because the edge on which c_{edge} is to be found is known by its location in the

[6]It may also be desirable to halt refinement after a maximum number of nodes allowed for the display grid have been inserted. In this case, some consideration should be given to the order in which computational elements are checked for display error.

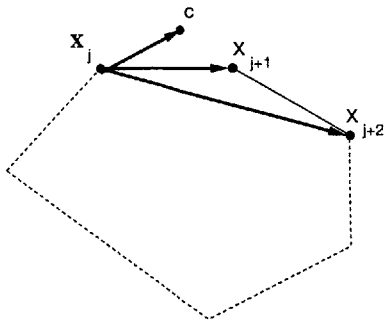

Figure 4-6: Locating a point in a grid.

list of quadrature points available for node insertion. The subelement containing c_{edge} can therefore be tracked logically as subdivision proceeds.

InsertNode(c)

1. For each subelement in the computational element:

   - If subelement circumcircle contains c, Then destroy subelement and note that its faces will need to be reconnected.

2. For each face to be reconnected

   - If the face connects two destroyed subelements, destroy the face (remove it from the list of faces to be reconnected).
   - If the node to be inserted is on the face, destroy the face (remove it from the list of faces to be reconnected).

3. Connect c to each node of each face that needs reconnection.

More formally, the node insertion process follows [23]. Let $\mathcal{S}$ be the set of elements of triangulation $\mathcal{T}$ whose circumcircle contains point c. Let $F_1 \ldots F_n$ be the faces in $\mathcal{S}$, excluding faces connecting two elements in $\mathcal{S}$. Then the new triangulation, which will be Delaunay, is

$$\mathcal{T}' = (\mathcal{T} - \mathcal{S}) \cup \{F_j, x\}_j, \qquad 1 \leq j \leq n. \tag{4.4}$$

The elements $\{F_j, x\}_j$ are reconnected so as to have positive area. This algorithm assumes that all node insertions will be within an existing linear display element. For the cases con-

sidered here, the first display element always encompasses the entire computational element, therefore all quadrature points, and this is always the case. See Section 6.2.2.

After one of the refinement exit conditions has been satisfied work moves on to the next computational element. When each computational element has been examined, the display grid is rechecked for error using the same quadrature rule. On the recheck, however, the quadrature points are selected for each display element, not merely for each computational element. Thus the recheck examines locations not previously considered for node insertion. This recheck may therefore reveal points in the display grid with more than E_{tol} error. It also allows a non-zero interior error to be calculated even if nodes were inserted at each *computational* quadrature point.

Chapter 5

Visualization Results

The new adaptive refinement algorithm is compared to the uniform, isotropic refinement algorithm in various test cases. For all cases, the following test conditions apply. Density is the state variable used for the error estimates and contour plots. The locations available for node insertion are the quadrature points of the computational element according to the maximum available quadrature rule (20 points on an edge, 42 in an interior). The locations checked for error are the quadrature points of each linear display element (see Section 4.3, end).

5.1 Supersonic Inviscid Diamond Airfoil

The two dimensional $M = 1.5$ case from Section 4.1 is revisited with the adaptive display method. The user-specified tolerance, E_{tol}, is varied by factors of 10 from 1×10^{-1} to 1×10^{-5}. The grids and resulting non-dimensional density contour plots with the four largest tolerances are shown in Figures 5-1.

The tolerance of 1×10^{-2} provides the most directed refinement. Tolerances smaller than this seem to pick up noise, and the tolerance an order of magnitude larger inserts only a few nodes above the minimum. Note also that the display grids appear denser along the original edges of the computational grid because 20 quadrature points are available for node insertion on each original edge[1].

Figure 5-2(c) compares the maximum point-wise display error, E_∞, and the total dis-

[1] A refined algorithm might ensure that quadrature points are more evenly distributed.

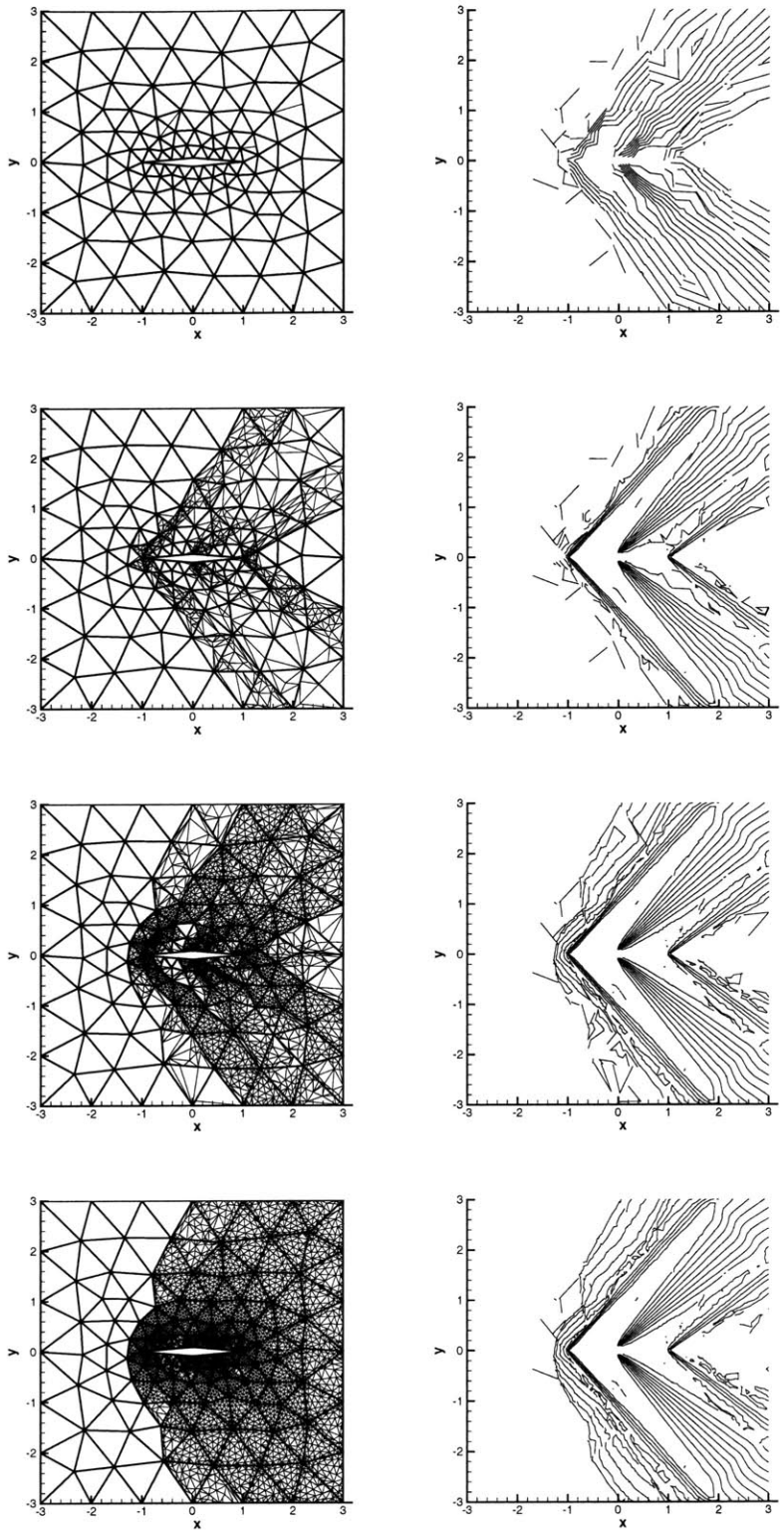

Figure 5-1: Adaptive subdivision with 10 contour levels of ρ/ρ_∞ between 0.84 and 1.2; $E_{\text{tol}} = 1 \times 10^{-1}$, 1×10^{-2}, 1×10^{-3}, and 1×10^{-4}, top to bottom. Number of nodes, top to bottom: 640, 1,508, 5,618, and 11,375.

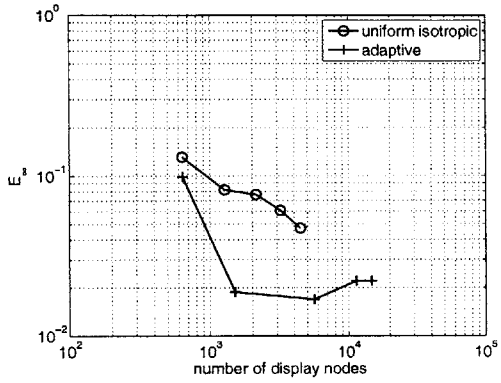

(a) Maximum pointwise error, estimated over quadrature points of linear display elements

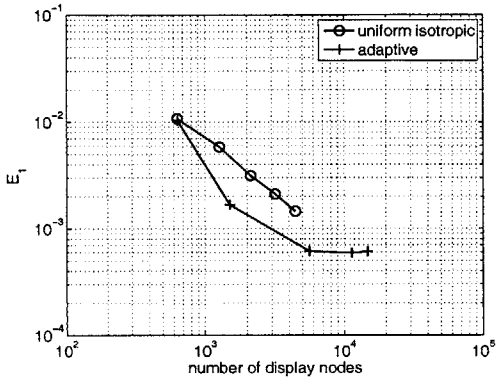

(b) Total error, estimated over quadrature points of linear display elements

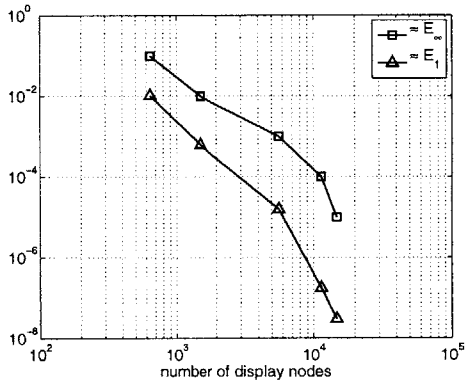

(c) Maximum pointwise and total errors, estimated over quadrature points of computational element only

Figure 5-2: Error as a function of display nodes for the $M = 1.5$ diamond airfoil grid

play error, E_1, against the number of nodes inserted, as estimated by considering *only* the quadrature points of the *computational element*, at which display nodes may be inserted. The data points correspond to the same five error tolerances used for the contour plots. This plot merely demonstrates that the algorithm is functioning properly: the E_∞ estimate is always below the user-specified tolerance, and the E_1 estimate tends to zero as nodes are inserted at every quadrature point. More accurate estimates are made by considering the quadrature points of all the *linear display elements*. Since the uniform, isotropic method and the adaptive method will have different linear display elements, these estimates will be slightly different between methods. It is expected, however, that they will still be comparable, and that the relative trends between the methods will still be observable, provided there is sufficient sampling within subelements[2]. The adaptive method is compared against the uniform, isotropic method using these estimates in Figures 5-2(a) and 5-2(b). The uniform isotropic data points correspond to the p^d subdivisions for linear through fifth-order polynomials: 3, 6, 10, 15, and 21 display nodes per element. The rest of the discussion considers only these more accurate estimates.

For the adaptive method, the sharp jump in the quality of the contour plots between tolerances of 1×10^{-1} and 1×10^{-2} coincides with the sharp reduction in E_∞ and E_1. The leveling off of these estimates is attributed to a limitation of the algorithm: nodes can be inserted only at the predetermined quadrature points. This makes it possible to refine a region as much as allowed and yet still leave the largest error in a location between new display nodes. In this case, for instance, E_∞ occurs on a shock in a computational element with a highly curved solution. Display nodes are inserted everywhere in the computational element, and the point-wise error is reduced, but a point between nodes still has the largest error in the grid. The solution continues to be improved elsewhere even though this particular error estimate is now fixed. This limitation would be removed by recursively refining display elements, see Section 6.2.2. The slight increase of E_∞ with number of display nodes is attributed to the better detection that comes with increased subdivision. E_∞ can be found only among quadrature points of linear display elements, so refining the display also refines the approximation to the true maximum point-wise error. Despite the observed limitation,

[2]It is unclear whether this disadvantages the adaptive method, which will tend to cluster subelements in high error regions.

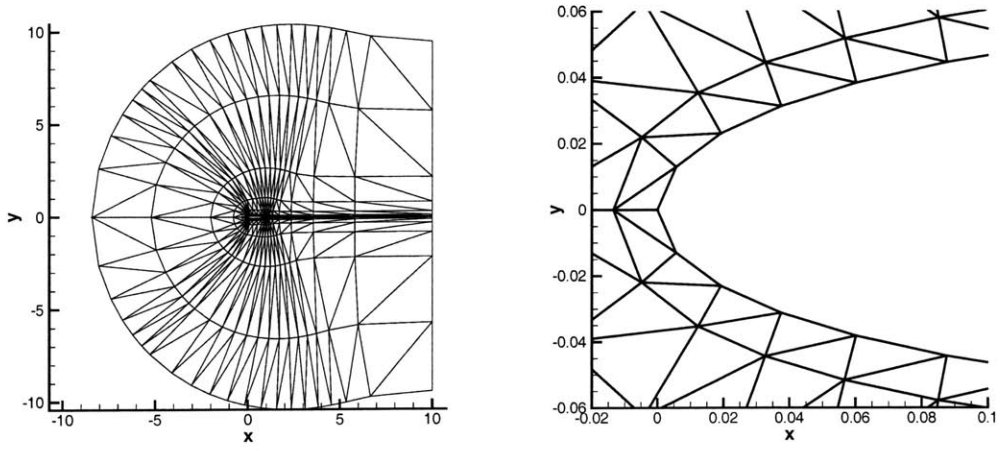

(a) NACA Grid

(b) NACA Grid, leading edge, linear display without subdivision

Figure 5-3: NACA airfoil

there are a range of error tolerances for which the adaptive algorithm is superior to uniform, isotropic refinement.

5.2 Subsonic Viscous Airfoil

It is worth examining the behavior of this algorithm on a completely smooth flow. The test case is a $q = 3$, NACA 0012 airfoil described by the grid in Figure 5-3(a) [49], with a $p = 3$ subsonic flow solution. The minimum number of nodes required to display the grid is 1920.

Plots of E_∞ and E_1 against the total number of display nodes are shown in Figure 5-4. The uniform, isotropic data points again correspond to linear through fifth order subdivisions of p^d elements. The adaptive display error tolerances used are 1×10^{-2}, 5×10^{-3}, 1×10^{-3}, 5×10^{-4}, 1×10^{-4}, and 1×10^{-5}. Figure 5-4(c) shows that the algorithm is working properly (see previous section). Considering the more accurate estimates in Figures 5-4(a) and 5-4(b), it is again apparent that the E_∞ error is greatly reduced by the new method with only a few nodes more than the minimum. This time, however, the total error is not reduced as quickly as in the uniform, isotropic case.

Figures 5-5 and 5-6 explain this difference by examining contour plots of the leading

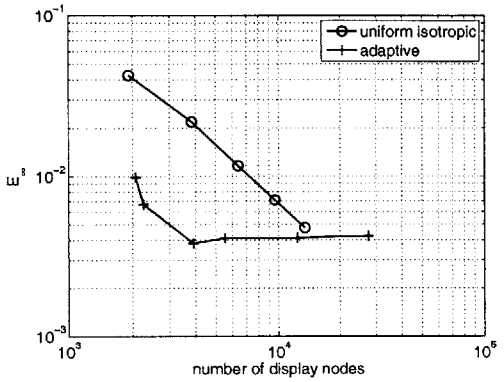

(a) Maximum pointwise error, estimated over quadrature points of linear display elements

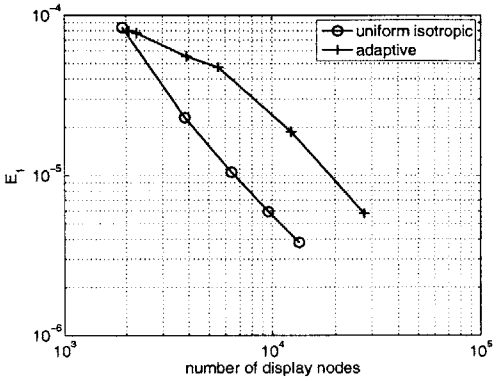

(b) Total error, estimated over quadrature points of linear display elements

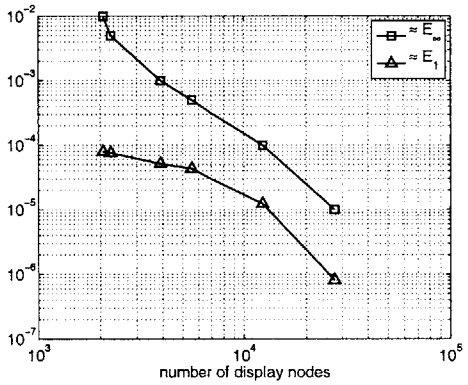

(c) Maximum pointwise and total errors, estimated over quadrature point of computational element only

Figure 5-4: Error as a function of display nodes for the subsonic NACA airfoil grid

edge and far-field flows displayed with comparable numbers of nodes. Figure 5-5 shows the results of the adaptive method, with 3906 nodes, and the uniform, isotropic display method, with 3840 nodes, at the leading edge and far from the airfoil. In the adaptive case, the boundary layer error is larger than the tolerance, such that nodes are inserted here, Figure 5-7(b). Adaptive refinement produces smooth boundary layer contours, especially in the transition between the boundary layer and the outside flow. This is in contrast to the far-field, which has a small point-wise display error (smaller than the tolerance), which is nevertheless large enough to produce poorly resolved, scalloped contours. On the other hand, uniform, isotropic refinement does not produce smooth transition contours between the boundary layer and the outside flow. Its nodes are nevertheless useful elsewhere: they produce smoother contours far from the airfoil. In fact, the uniform, isotropic method, by virture of uniform and error-independent node insertion, results in smaller pointwise display error in the farfield for a given number of nodes. This, combined with the fact that the E_1 estimate is area-weighted, reduces the E_1 error more quickly than the adaptive method.

Figure 5-6 shows that when the error tolerance is reduced to 1×10^{-4}, the adaptive method refines the far-field enough to smooth the contours around the airfoil. The boundary layer is not noticeably changed, as its primary errors were corrected with the larger error tolerance. The uniform, isotropic method, with $\{p = 5\}^d$ subdivisions, now has enough nodes per element in the boundary layer to produce smooth contours, nearly on par with the adaptive method. Its far-field contours are now very smooth.

These differences are captured in the relative differences between the E_∞ and E_1 estimates. The E_∞ estimate gives a good indication of boundary layer resolution, for which point-wise error is initially large. The fact that it levels off is again attributable to the location of the maximum point-wise error, in the boundary layer near the trailing edge, which is inaccessible to the algorithm (described in the previous Section 5.1, see also Section 6.2.2). Unlike the E_∞ estimate, the E_1 estimate is dominated by the larger flow features, via the area scaling in the estimate, and gives a good indication of the display of the larger contours. Figure 5-4(b) shows that the adaptive method ultimately improves the E_1 error at the same rate as the uniform, isotropic method, but with offset in the total number of display nodes. The offset is due to the nodes that must be inserted in the boundary layer before the adaptive method gets to refine the larger flow field. This large-scale refinement happens for

tolerances tighter than approximately 5×10^{-4}.

As an aside: With no subdivision, a zoom on the leading edge, as in Figure 5-3(b), shows a piece-wise linear display of the cubic airfoil surface. Note that the adaptive refinement procedure, which first inserts nodes in the boundary layer, Figures 5-7(a) and 5-7(b), respects the higher order geometry, effectively improving its display along with that of the solution.

5.3 Hypersonic Viscous Cylinder

The adaptive refinement method is applied to the benchmark case from Chapter 3 with a $p = 4$ solution. The adaptive method is used with tolerances 5×10^{-1}, 1×10^{-1}, 5×10^{-2}, and 1×10^{-2}. The uniform isotropic method is used with linear through fifth order subdivisions of p^d elements. Plots of E_∞ and E_1 against number of display nodes are shown in Figure 5-8. In this case, although the maximum pointwise error appears to spike for the tightest tolerance with the adaptive method, these curves are largely flat (see scale). The strong shock has a number of points with large error and these are not easily correctable with either method. The total error shows the same offset as in the subsonic viscous case, again because many nodes are inserted in the high gradient regions for a given error tolerance before the larger flow field is refined.

The grid with the adaptive method and $E_{\text{tol}} = 5 \times 10^{-2}$, which produces the lowest pointwise error of those considered here, is shown in Figure 5-10. This grid has 54,640 nodes; the minimum required is 23,040. Boundary layer elements are too narrow to be shown clearly, although there is refinement here as well as in the shock. A uniform, isotropically displayed grid with a similar number of nodes, 46,080, is shown in Figure 5-9. The adaptive method has clearly focused refinement on high gradient regions of interest.

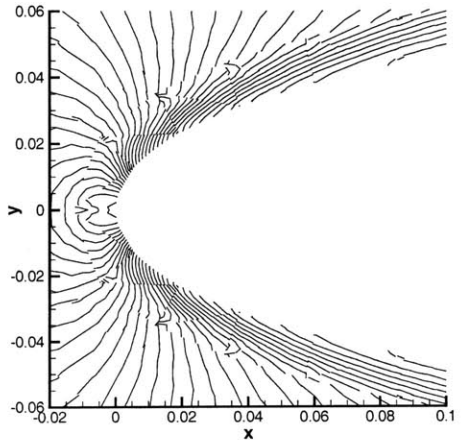

(a) Adaptive

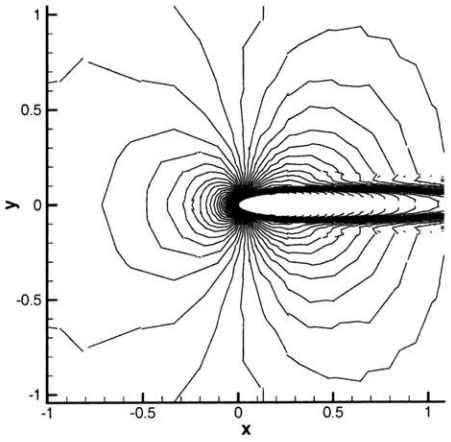

(b) Adaptive

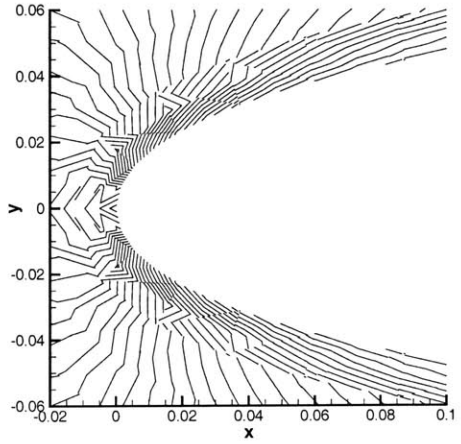

(c) Uniform, isotropic

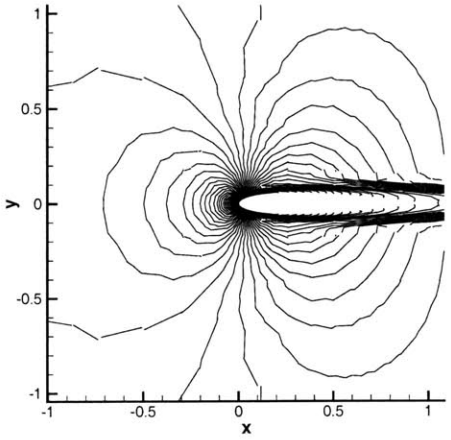

(d) Uniform, isotropic

Figure 5-5: Contour plots of ρ/ρ_∞ between 0.84 and 1.2 for leading edge flow (in 50 levels) and entire flow (in 100 levels) using both methods. Adaptive: 3,906 display nodes, $E_{\text{tol}} = 1 \times 10^{-03}$. Uniform, Isotropic: 3,840 display nodes, $\{p = 2\}^2$ subelements per computational element.

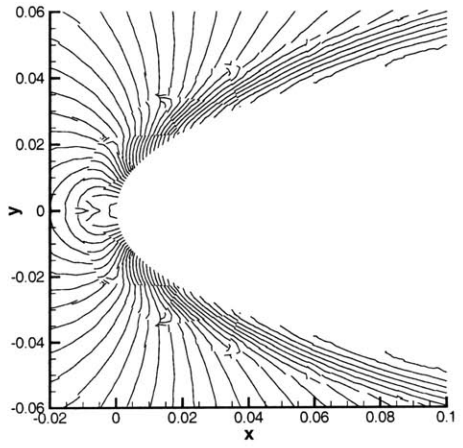

(a) Adaptive

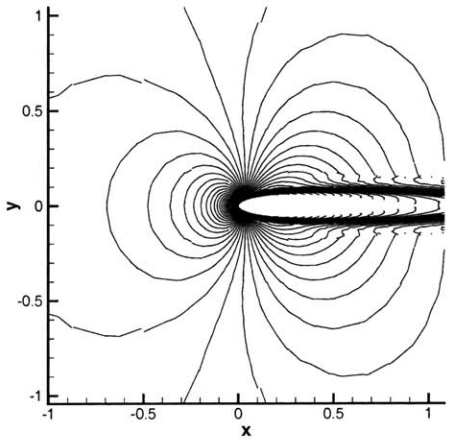

(b) Adaptive

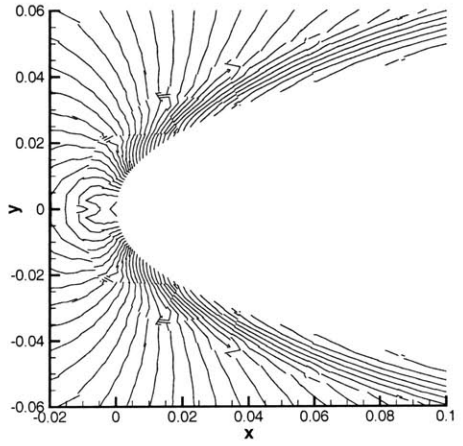

(c) Uniform, isotropic

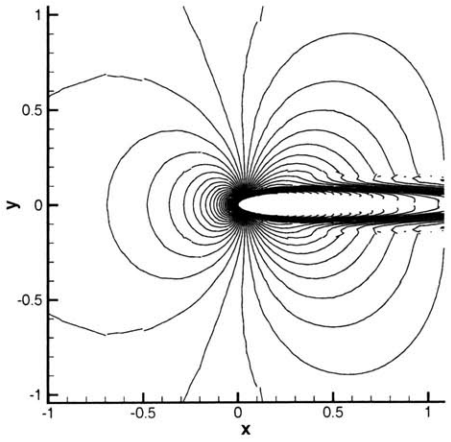

(d) Uniform, isotropic

Figure 5-6: Contour plots of ρ/ρ_∞ between 0.84 and 1.2 for leading edge flow (in 50 levels) and entire flow (in 100 levels) using both methods. Adaptive: 12,330 display nodes, $E_{\text{tol}} = 1\times10^{-04}$. Uniform, Isotropic: 13,440 display nodes, $\{p = 5\}^2$ subelements per computational element.

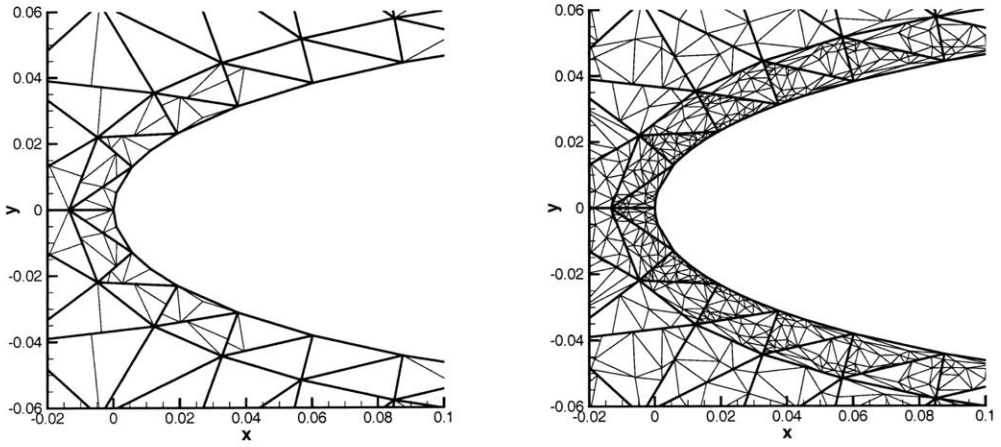

(a) Leading edge, adaptive display, $E_{\text{tol}} = 1 \times 10^{-2}$.

(b) Leading edge, adaptive display, $E_{\text{tol}} = 1 \times 10^{-3}$.

Figure 5-7: Examples of adaptive boundary layer refinement

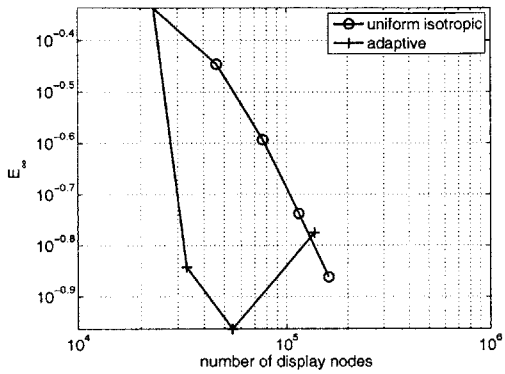

(a) Maximum pointwise error, estimated over quadrature points of linear display elements

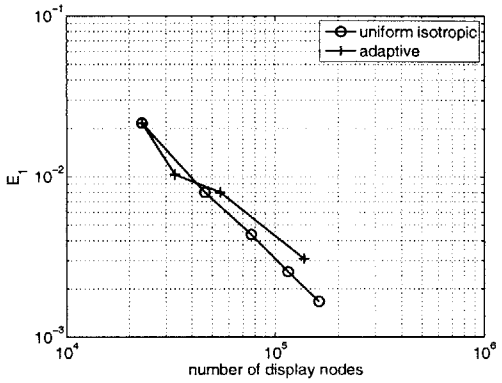

(b) Total error, estimated over quadrature points of linear display elements

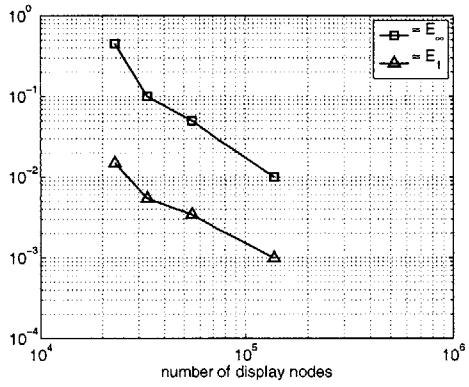

(c) Maximum pointwise and total errors, estimated from quadrature points of computational element only

Figure 5-8: Error as a function of display nodes for the hypersonic cylinder grid

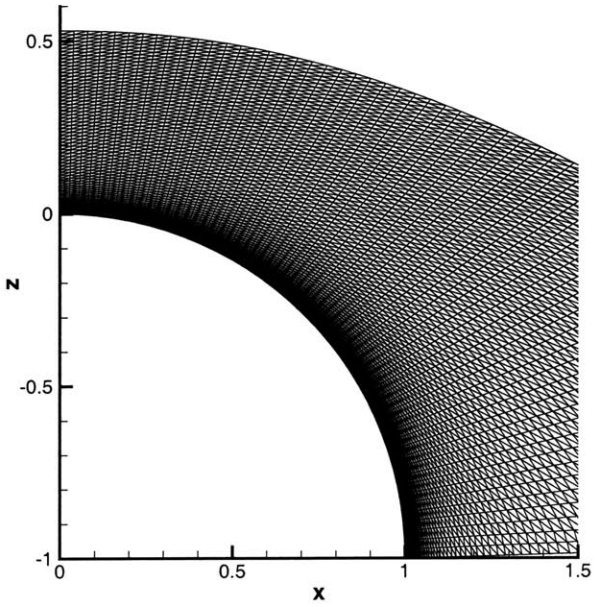

Figure 5-9: The hypersonic display grid, isotropic subdivision into $p^d = 4$ elements, 46,080 nodes, $E_\infty = 0.36$, $E_1 = 8 \times 10^{-3}$.

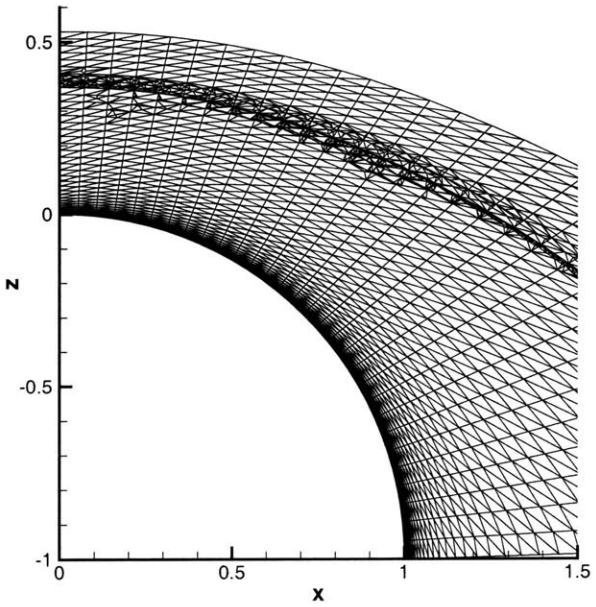

Figure 5-10: The hypersonic display grid, adaptive subdivision with $E_{\text{tol}} = 5 \times 10^{-2}$, 54,640 nodes, $E_\infty = 0.11$, $E_1 = 8 \times 10^{-3}$ (same as uniform, isotropic case).

Chapter 6

Conclusions

6.1 Discontinuous Galerkin Finite Element Method

Offered below are concluding remarks about the discontinuous Galerkin implementation used here, along with recommendations for future work.

6.1.1 Remarks on DG for Hypersonics

As implemented, the higher-order DG discretization can be used to simulate hypersonic perfect gas flows. While the results appear promising for average values, oscillations within elements for skin friction and heat transfer are significant. This issue remains to be addressed. The oscillations may be related to oscillations observed in the flow behind the shock, although the evidence is circumstantial. It may be a number of factors used in computing these surface quantities, for which gradients of the solution are required. Looking past the current challenges, there are also a few improvements to be made to other aspects of this DG method.

6.1.2 Future Work

Improve Shock Capturing

The shock capturing algorithm may perform less well than the same Laplacian artificial viscosity scheme in [45]. Typically shocks are being captured over a few elements – for low p, more than six, for $p = 4$ approximately three; Persson and Peraire indicate that it is possible to do better. (It would be worthwhile to compare results by matching their inviscid

test cases.) Additionally, other indicators might be used. Preliminary experimentation with a resolution-based indicator, also in [45], suggests that it will target individual elements with shocks more specifically than the entropy residual indicator. This might help reduce smearing. Another idea that may be worth pursuing is the addition of artificial viscosity in a directional sense. An approach like that of [50] reduces oscillations by smoothing across isovalues of the flow rather than across the shock. The most important modification for the future may be an algorithm to automatically adjust the cap and gain on the shock indicator. The current need to manually tune these quantities for each problem greatly increases the time required to reach a solution with strong shocks.

Improve Grid Generation with Curved Geometry

Another generally worthwhile improvement would be in the area of higher order mesh generation. The difficulty in matching the Langley test case with higher order geometry is highlighted by Figure 6-1: if a polynomial approximation to a geometric boundary overlaps an element edge, as shown at left, which can happen for high aspect ratio elements, the curvature of that edge must be propagated throughout the domain, at least until some transition point when linear elements can again be used. Otherwise, these elements must be reduced in aspect ratio by local refinement. For the $q = 2$ grid used in this work, the higher order geometry was propagated throughout the entire grid (rather than looking for a suitable cut-off location). In general, an approach like this inserts more higher order nodes than necessary to represent a boundary, unnecessarily increasing the cost of a computation. An algorithm might be developed that would automatically distribute the higher order geometry only as far as necessary to prevent invalid elements.

Improve Robustness of Solution Initialization

It was mentioned in Section 3.2.2 that the Reynolds number must be kept low for the first step of the solution procedure. The reason for this is at the moment empirical, but it is believed to be tied to boundary layer resolution. Starting the solution process from a free-stream initialization at high Re results in an instability where the boundary layer hits the extrapolation boundary condition. It manifests itself in the same way as a shock instability, in that Mach number spikes, although it cannot be the same because it occurs even at $p = 0$,

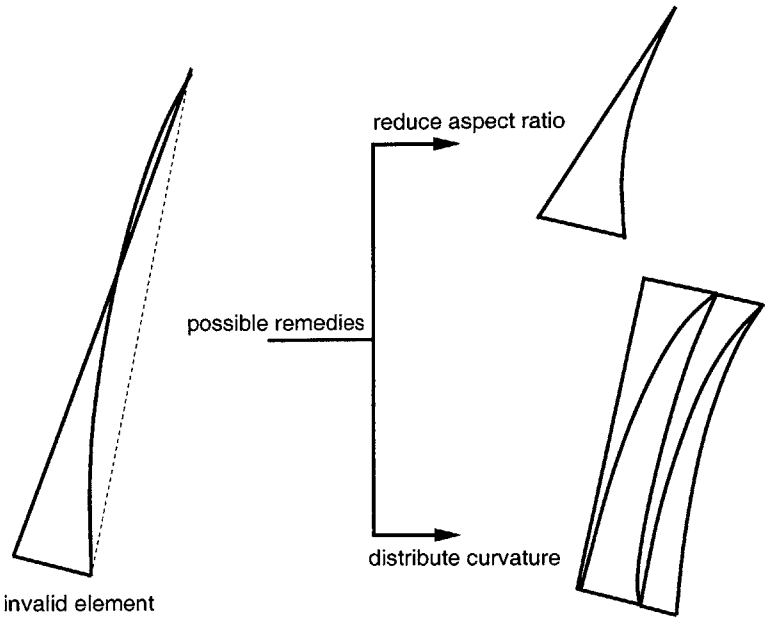

Figure 6-1: Special consideration is required for higher order, high aspect ratio elements. There are two workarounds.

a non-dispersive discretization. Experience suggests considering the role Reynolds number has as a measurement of viscosity. At relatively lower-than-target Reynolds number a flow can be said to have relatively higher-than-target viscosity, therefore, thicker boundary layers, therefore, better resolution on a given grid. It may be that without this extra resolution, the boundary layers are poorly resolved, and as a result, trigger the aforementioned instability in the extrapolation boundary conditions.

This hypothesis is consistent with observations made when trying to "thin" the Langley grid for use with higher order elements[1]. Removal of elements near the cylinder face (coarsening in the radial direction) resulted in the same instability. If the problem persists a better theoretical justification would be appropriate.

Model High Temperature Effects

A next step for DG and hypersonics could be to model high temperature effects. It would require solving additional equations at each step for the reacting species. The current implementation is general enough to allow for additional equations, and plans for its immediate

[1]See previous section on higher order geometry.

future include adding a multi-species plasma model with space propulsion applications. The changes required to expand the code to chemically reacting flows would complement the plasma additions. The original benchmark using the LAURA code presents data for a multiple species reacting flow and would provide another valuable benchmark in the future.

6.2 Visualization

Offered last are concluding remarks about the adaptive display algorithm, along with recommendations for future work.

6.2.1 Comments on the Algorithm

The adaptive algorithm improves the display of higher order DG solutions over the uniform, isotropic method. The improvement can be viewed as either greater efficiency or greater accuracy: for a given accuracy, the adaptive display requires fewer nodes; alternatively, for a given number of nodes, the adaptive display has a smaller maximum point-wise error and total error. The one exception to this is when large-scale flow features with small point-wise error are intended to be resolved preferentially to high-gradient features. In this case, the adaptive algorithm simply cannot get to these large-scale features without first inserting many nodes into regions like boundary layers and shocks. Oftentimes, however, what matters most is the accuracy of the display in sharp transition regions. For these cases, the adaptive algorithm is a better method.

The three test cases examined suggest a "best performing" non-dimensional error tolerance of $\mathcal{O}(1 \times 10^{-2})$. With this value, the adaptive algorithm achieves the greatest reduction in error for the same number of nodes as a uniform, isotropic refinement.

6.2.2 Future Work

A number of improvements can be made to make this algorithm better suited for common use.

Permit Outwardly Curved Computational Elements

A key assumption in the node insertion algorithm is that all quadrature points can be found within an existing linear display element. For the kinds of test cases considered here — airfoils, cylinders — this is valid. If a computational element is curved outside of its shadow, however, this is not generally the case. It is not a problem when this happens and the point is known to lie on an edge; the logic used to locate edge points within linear display elements is generally valid. The problem arises when interior points, which have no edge association, fall outside any linear display element. These points cannot be located in a linear display element for error checking; the linear solution is not even strictly defined at these points. In an extreme case, these points cannot even be located by element circumcircles for Delaunay node insertion. There are logic checks that can repair this deficiency, although they have not been pursued for this work.

Recursively Refine Linear Display Elements

It is possible to insert a node at every computational quadrature point and still have a point in the grid with a demonstrably and unacceptably large display error. This is observed as a leveling off of the E_∞ and E_1 error estimates past a certain number of display nodes. It occurs because the possible sites of node insertion are fixed; if nodes have been inserted at quadrature points all around the location of maximum error, nothing more can be done for this part of the grid, and this maximum error remains for all further refinements (which happen elsewhere).

The problem can be overcome by recursion of the element refinement algorithm on linear subelements. Once a computational element is refined, the linear subelement with the largest error can be treated as the next computational element, and the node insertion process can be repeated on its new set of quadrature points. This exposes potentially unlimited locations for node insertion. The difficulty here is when the linear subelement is intended to represent part of a higher order edge. In this case, the linear quadrature points now available for node insertion may not respect the original higher order geometry. A modification to straight recursion would be required to retain the higher order geometry.

Find a General Error Tolerance

The user-specified error tolerance is currently non-dimensional. This makes the error tolerance a "percent error" that has the same meaning regardless of the units used in a solution; it therefore produces similar results across a wide variety of solutions. The non-dimensionalization assumes that the average value of the solution variable being checked is never zero in an element. If it is zero, the non-dimensional error will be infinite, and a problem-specific dimensional form must be used. A non-dimensionalization that is not vulnerable to a bad choice of solution variable would improve the general utility of the algorithm.

Refine in Three Dimensions

The refinement algorithm will be most beneficial when it is implemented in three dimensions, for which uniform, isotropic subdivision can be particularly inefficient. This was not done for this work due to time constraints. The primary changes required will be to adapt the triangulation routine to connect nodes with 3D element faces, and to generalize the bookkeeping that tracks the original computational face from which a linear display face has been created (this information is needed by the node insertion algorithm).

Bibliography

[1] H. Julian Allen and Alfred J. Eggers Jr. A study of the motion and aerodynamic heating of ballistic missiles entering the Earth's atmosphere at high supersonic speeds. Technical Report 1381, NACA, Washington, D.C., 1958.

[2] John D. Anderson. *Hypersonic and High Temperature Gas Dynamics.* McGraw-Hill, New York, 1989.

[3] John D. Anderson. *Computational Fluid Dynamics.* McGraw-Hill, Inc., New York, NY, 1995.

[4] F. Bassi and S. Rebay. High-order accurate discountinuous finite element solution of the 2-D Euler equations. *J. Comput. Phys.*, 138:251–285, 1997.

[5] F. Bassi and S. Rebay. An implicit high-order discontinuous Galerkin method for the steady state compressible Navier-Stokes equations. In Papailiou; Tsahalis; Periaux; Hirsh; and Pandolfi, editors, *Computational Fluid Dynamics 98, Proceedings of the Fourth European Computational Fluid Dynamics Conference*, pages 1227–1233. Wiley, New York, 1998.

[6] F. Bassi and S. Rebay. GMRES discontinuous Galerkin solution of the compressible Navier-Stokes equations. In Karniadakis Cockburn and Shu, editors, *Discontinuous Galerkin Methods: Theory, Computation and Applications*, pages 197–208. Springer, Berlin, 2000.

[7] Scott A Berry, Thomas J. Horvath, and Brian R. Hollis. X-33 hypersonic boundary layer transition. *AIAA Journal*, 1999.

[8] J. P. Boris and D. L. Book. Flux corrected transport I, SHASTA, a fluid transport algorithm that works. *Journal of Computational Physics*, 11(1):38–69, 1973.

[9] Michael L. Brasher. Visualizing quadratic and cubic finite elements. Master's thesis, Massachusetts Institute of Technology, August 2004.

[10] P. G. Buning. Sources of error in the graphical analysis of CFD results. *Journal of Scientific Computing*, 3(2):149–164, 1988.

[11] A. Burbeau, P. Sagaut, and Ch.-H. Bruneau. A problem-independent limiter for high-order Runge-Kutta discontinuous Galerkin methods. *Journal of Computational Physics*, 169(1):111–150, 2001.

[12] Mark H. Carpenter and Jay H. Casper. Computational considerations for the simulation of discontinuous flows. In V. Venkatakrishnan and et al., editors, *Barriers and Challenges in Computational Fluid Dynamics*. Kluwer Academic Publishers, 1998.

[13] Jay Casper and Mark H. Carpenter. Computational considerations for the simulation of shock-induced sound. *SIAM Journal of Scientific Computing*, 1998.

[14] M. J. Castro-Diaz, F. Hecht, B. Mohammadi, and O. Pironneau. Anisotropic unstructured mesh adaptation for flow simulations. *International Journal for Numerical Methods in Fluids*, 1997.

[15] Langley Research Center. *Fully Unstructured Navier-Stokes (FUN3D) Product Manual*. National Aeronautics and Space Administration, Jan 2006. [Available online at http://larc.nasa.gov/].

[16] B. Cockburn and C. W. Shu. The Runge-Kutta local projection p^1-discontinuous Galerkin method for scalar conservation laws. *RAIRO Model Math. Anal. Numer.*, 25:337–361, 1991.

[17] Vit Dolejsi, Miloslav Feistauer, and Christoph Schwab. On some aspects of the discontinuous Galerkin finite element method for conservation laws. *Mathematics and Computers in Simulation*, 61(3):333–346, 2003.

[18] Peter A. Gnoffo et. al. Opportunities for breakthroughs in large-scale computational simulation and design. Technical Report NASA/TM-2002-211747, Langley Research Center, NASA, June 2002.

[19] Krzysztof J. Fidkowski. A high-order discontinuous Galerkin multigrid solver for aerodynamics applications. Master's thesis, Massachusetts Institute of Technology, June 2004.

[20] Krzysztof J. Fidkowski and David L. Darmofal. Development of a higher-order solver for aerodynamic applications. In *42nd AIAA Aerospace Sciences Meeting and Exhibit, Reno, Nevada,*. AIAA, January 2004. 2004-0436.

[21] Krzysztof J. Fidkowski, Todd A. Oliver, James Lu, and David L. Darmofal. p-multigrid solution of high-order discontinuous Galerkin discretizations of the compressible Navier-Stokes equations. *Journal of Computational Physics*, 207:92–113, 2005.

[22] Datta Gaitonde and J. S. Shang. Accuracy of flux-split algorithms in high-speed viscous flows. *AIAA Journal*, 31(7), July 1993.

[23] P. L. George. *Automatic Mesh Generation: Application to Finite Element Methods.* Wiley, Paris, 1991.

[24] Peter A. Gnoffo. Computational fluid dynamics technology for hypersonic applications. *AIAA/ICAS International Air and Space Symposium and Exposition, Dayton, Ohio*, July 2003. AIAA 2003-3259.

[25] Peter A. Gnoffo and F. McNeil Cheatwood. *User's Manual for the Langley Aerothermodynamic Upwind Relaxation Algorithm (LAURA).* Langley Research Center, National Aeronautics and Space Administration, April 1996. NASA Technical Memorandum 4674.

[26] Peter A. Gnoffo and Jeffery A. White. Computational aerothermodynamics simulation issues on unstructured grids. *AIAA Journal*, 2004.

[27] Henri Gouraud. Continuous shading of curved surfaces. *IEEE Transactions on Computers*, 1971.

[28] Robert Haimes. Techniques for interactive and interrogative scientific volumetric visualization. [Available online, http://raphael.mit.edu/visual3/visual3.html, Jan 2006].

[29] Robert Haimes. *Visual3 User's and Programmer's Manual.* Aerodynamics Computational Design Laboratory, Massachusetts Institute of Technology. [Available online, http://raphael.mit.edu/visual3/visual3.html, Jan 2006].

[30] Robert Haimes and David Darmofal. Visualization in computational fluid dynamics: A case study. In *IEEE Visualization*, 1991.

[31] Robert Haimes and Michael Giles. Visual3 – interactive unsteady unstructured 3D visualization. In *29th AIAA Aerospace Sciences Meeting, Reno, NV, Jan. 7-10*, 1991.

[32] Brian R. Hollis, Scott A Berry, and Thomas J. Horvath. X-33 turbulent aeroheating measurements and predictions. *AIAA Journal*, 2002.

[33] Loyd S. Swenson Jr., James M. Grimwood, and Charles C. Alexander. *This New Ocean: A History of Project Mercury.* National Aeronautics and Space Administration, 1989. Special Publication-4201. [Available online at http://www.hq.nasa.gov/office/pao/History/SP-4201/toc.htm, Jan 2006].

[34] L. Krivodonova, J. Xin, J.-F. Remacle, N. Chevaugeon, and J. E. Flaherty. Shock detection and limiting with discontinuous Galerkin methods for hyperbolic conservation laws. *Applied Numerical Mathematics*, 48(3):323–338, 2004.

[35] Aerospace Computational Design Laboratory. *Project-X User's Guide.* Department of Aeronautics and Astronautics, Massachusetts Institute of Technology, Nov 2005.

[36] Kelly R. Laflin, John C. Vassberg, Richard A. Wahls, Joseph H. Morrison, Olaf Brodersen, Mark Rakowitz, Edward N. Tinoco, and Jean-Luc Godard. Summary of data from the Second AIAA CFD Drag Prediction Workshop. Technical Report 2004-0555, AIAA, 2004.

[37] S. K. Lele. Compact finite difference schemes with spectral-like resolution. *J. Comput. Phys.*, 103:16–42, 1992.

[38] Randall J. LeVeque. *Numerical Methods for Conservation Laws.* Birkhäuser Verlag, Boston, 1992.

[39] David W. Levy, Thomas Zickuhr, John Vassberg, Shreekant Agrawal, Richard A. Wahls, Shahyar Pirzadeh, and Michael J. Hemsch. Data summary from the First AIAA Computational Fluid Dynamics Drag Prediction Workshop. *Journal of Aircraft*, 40(5):875–882, 2003.

[40] H. W. Liepmann and A. Roshko. *Elements of Gas Dynamics.* Dover Publications, Inc., Mineola, NY, 1985.

[41] G. Moretti and M. Abbett. A time dependent computational method for blunt body flows. *AIAA Journal*, 1966.

[42] US Centennial of Flight Commission. Evolution of technology: Early reentry vehicles. [Available online at http://www.centennialofflight.gov, Jan 2006].

[43] Todd A. Oliver. Multigrid solution for high-order discontinuous Galerkin discretizations of the compressible Navier-Stokes equations. Master's thesis, Massachusetts Institute of Technology, August 2004.

[44] OpenGL. OpenGL. [Available online at http://www.opengl.org, Jan 2006].

[45] P.-O. Persson and J. Peraire. Sub-cell shock capturing for discontinuous Galerkin methods. In *44th AIAA Aerospace Sciences Meeting and Exhibit*, Jan 2006.

[46] Jianxian Qiu and Chi-Wang Shu. Hermite WENO schemes and their application as limiters for Runge-Kutta discontinuous Galerkin method: One-dimensional case. *Journal of Computational Physics*, 193(1):115–135, 2004.

[47] Jianxian Qiu and Chi-Wang Shu. Hermite WENO schemes and their application as limiters for Runge-Kutta discontinuous Galerkin method II: Two dimensional case. *Computers and Fluids*, 34:642–663, 2005.

[48] James J. Quirk. A contribution to the great Riemann solver debate. In M. Yousuff Hussaini, Bram van Leer, and John Van Rosendale, editors, *Upwind and High-Resolution Schemes*, pages 550–569. Springer, New York, 1997.

[49] R. Radespiel and R. C. Swanson. Personal communication. via Todd Oliver, Massachusetts Institute of Technology, Aerodynamics Computational Design Laboratory.

[50] L. Remaki, H. Beaugendre, and W. G. Habashi. ISOD – an anisotropic isovalue-oriented diffusion artificial viscosity for the Euler and Navier-Stokes equations. *Journal of Computational Physics*, (186):279–294, 2003.

[51] G. R. Richter. An optimal-order error estimate for the discontinuous Galerkin method. *Math. Comp.*, 50:75–88, 1988.

[52] Hermann Schlichting. *Boundary Layer Theory.* McGraw-Hill Book Company, Inc., New York, seventh edition edition, 1979.

[53] Sung soo Kim, Chongam Kim, Oh-Hyun Rho, and Seung Kyu. Cures for the shock instability: Development of a shock-stable Roe scheme. *Journal of Computational Physics*, 2003.

[54] P. K. Sweby. High resolution schemes using flux limiters for hyperbolic conservation laws. *SIAM Journal on Numerical Analysis*, 21(5):995–1011, 1984.

[55] Christoph W. Ueberhuber. *Numerical Computation 2: Methods, Software, and Analysis.* Springer-Verlag, Berlin, Germany, 1997.

[56] Bram van Leer. Towards the ultimate conservative difference scheme. II - Monotonicity and conservation combined in a second order scheme. *Journal of Computational Physics*, 14:361–370, 1974.

[57] Bram van Leer. Towards the ultimate conservative difference scheme. III - upstream-centered finite-difference schemes for ideal compressible flow. *Journal of Computational Physics*, 23:263–275, 1977.

[58] Bram van Leer. Towards the ultimate conservative difference scheme. V - a second-order sequel to Godunov's method (for ideal compressible flow). *Journal of Computational Physics*, 32:101–136, 1979.

[59] John C. Vassberg, Mark A. DeHaan, and Tony J. Sclafani. Grid generation requirements for accurate drag predictions based on OVERFLOW calculations. *AIAA*, 2003. 2003-4124.

[60] Luiz Velho, Luiz Henrique de Figueirido, and Jonas Gomes. A unified approach for hierarchical adaptive tesselation of surfaces. *ACM Transacations on Graphics*, 1999.

[61] David Anthony Venditti. *Grid Adaptation for Functional Outputs of Compressible Flow Simulations.* PhD thesis, Massachusetts Institute of Technology, June 2002.

[62] V. Venkatakrishnan. Convergence to steady state solutions of the Euler equations on unstructured grids with limiters. *Journal of Computational Physics*, 118:120–130, 1995.

[63] M. R. Visbal and D. V. Gaitonde. On the use of higher-order finite-difference schemes of curvilinear and deforming meshes. *Journal of Computational Physics*, 181:155–185, 2002.

[64] J. von Neumann and R. D. Richtmyer. A method for the numerical calculation of hydrodynamic shocks. *Journal of Applied Physics*, 21:232–237, 1950.

[65] Z. J. Wang. Spectral (finite) volume method for conservation laws on unstructured grids. Basic formulation. *J. Comput. Phys.*, 178:210–251, 2002.

[66] John F. Wendt. External hypersonic aerodynamics: State-of-the-art and future perspective. *Advisory Group for Aerospace Research and Development, Working Group 18.* North Atlantic Treaty Organization.

[67] David F. Wiley. *Approximation and Visualization of Scientific Data Using Higher Order Elements.* PhD thesis, University of California, Davis, 2003.

[68] Nail K. Yamaleev and Mark H. Carpenter. On accuracy of adaptive grid methods for captured shocks. *Journal of Computational Physics*, 2002.

[69] Y. Zhou, M. Garland, and R. Haber. Pixel-exact rendering of spacetime finite element solutions. *Proceedings of IEEE Visualization 2004*, October 2004.

[70] D. W. Zingg, S. De Rango, M. Nemec, and T. H. Pulliam. Comparison of several spatial discretizations for the Navier-Stokes equations. *J. Comput. Phys.*, 160:683–704, 2000.